Contrast and Volume Rate Enhancement of 3-D Ultrasound Imaging Using Aperiodic Plane Wave Angles: A Simulation Study

Sua Bae, *Member, IEEE*, Jiwon Park, *Member, IEEE*, and Tai-Kyong Song, *Member, IEEE*

***Abstract*— Three-dimensional plane wave imaging (PWI) with a 2-D array has been studied for ultrafast volumetric imaging in medical ultrasound. Compared to 2-D PWI, 3-D PWI requires the transmission of an increased number of plane waves (PWs) to scan a volume of interest and achieve transmit dynamic focusing in both the lateral and elevational directions. To reduce the number of PW angles for a given 2-D angular range by mitigating the grating lobe level, we propose two aperiodic patterns of PW angles: concentric rings with a uniform radial interval and the well-known sunflower pattern. Both patterns are validated to provide uniform angle distributions without regular periodicity, and thereby reduce the grating lobe level compared to a periodic angle distribution with the same number of PW angles. Simulation studies show that the aperiodic patterns enhance the contrast of B-mode images by approximately 3–6 dB over all depths. This enhancement implies that the aperiodic angle sets can increase the volume rate by approximately 2–6 times compared to the periodic angle set at the same contrast and spatial resolution.**

***Index Terms*— 2-D matrix array ultrasonic transducer, 3-D ultrasound (US) imaging, plane wave imaging (PWI).**

I. Introduction

ULTRASOUND (US) volumetric (3-D) imaging has been shown to offer advantages in relation to traditional 2-D US imaging in various clinical applications [1], [2]. First, arbitrary image planes, including any desired image plane that is difficult to capture in the 2-D US, can be obtained via 3-D US imaging. Second, 3-D US imaging can accurately measure both the 2-D and 3-D anatomical information required to examine anomalies, such as in gynecologic ultrasonography, whereas 2-D US imaging systems rely on a simple geometric model for extrapolation from 2-D to 3-D anatomy [3], [4]. Third, volumetric scanning is essential for various applications in functional and molecular US imaging. In echocardiography, the detection of 3-D heart wall motion and the estimation of the blood ejection volume can be performed much more accurately via volumetric imaging than via 2-D scanning [5]–[7]. In addition, observations of the 3-D propagation of shear waves in soft tissues lead to more accurate measurements of tissue elasticity [8]. Three-dimensional US imaging is also imperative for functional brain imaging and photoacoustic imaging [9], [10].

In those applications, the volume rate and the spatial resolution are perhaps the two most important factors determining the quality and applicability of US 3-D imaging. In the traditional method of real-time 3-D imaging, a series of multiple image slices are obtained by mechanically wobbling or moving a 1-D array transducer. In this case, dynamic focusing is achieved only in the lateral direction, and fixed focusing is employed in the elevational direction using an acoustic lens. This process severely degrades the spatial resolution, particularly when observing images on reconstructed planes that are not parallel to the acquired image slices. Moreover, wobbling 1-D arrays cannot provide high volume rates because they can only scan image slices sequentially, one after the other.

Two-dimensional matrix probes have attracted considerable attention because they can overcome the two drawbacks of mechanical 3-D scanning using 1-D arrays. In theory, matrix probes can focus US waves dynamically along both the lateral and elevational directions because they consist of array elements arranged in both the dimensions. In addition, a 2-D matrix array enables ultrafast volumetric imaging by employing fast imaging techniques, such as parallel beamforming and synthetic transmit focusing (STF), and plane wave imaging (PWI) techniques for the simultaneous acquisition of a large number of scanlines on multiple planes.

Parallel beamforming techniques, such as the multiline acquisition (MLA) [11]–[15] and multiline transmit (MLT) [16]–[19] methods, have been shown to improve the volume rate. However, these approaches present limitations on the number of scanlines that can be simultaneously obtained without causing noticeable degradation in the image quality. Moreover, such parallel beamforming techniques allow for dynamic focusing only on reception.

Certain STF techniques developed for 1-D array imaging that utilize plane waves (PWs) or diverging beams have also been adopted for ultrafast 3-D (or 4-D) US imaging with 2-D arrays [2], [20]–[24]. Such 3-D STF methods can achieve transmit (TX) dynamic focusing via the coherent compounding of unfocused waves at all imaging points. In the case of 3-D STF using PWs, PW angles are distributed in a 2-D coordinate system, which is defined by the lateral and elevational directions for synthetic TX focusing in every direction in the 2-D space.

Manuscript received June 10, 2019; accepted July 23, 2019. Date of publication July 31, 2019; date of current version October 24, 2019. This work was supported by the R&D program of MOTIE/KEIT (10076675, Development of MR Based High Intensity Focused Ultrasound Systems for Brain and Urinogenital Diseases), South Korea. This research was also supported by Global Ph.D Fellowship Program through the National Research Foundation of Korea (NRF) funded by the Ministry of Education (2015H1A2A1031492), South Korea. *(Corresponding author: Tai-Kyong Song.)*

S. Bae and T.-K. Song are with the Department of Electronic Engineering, Sogang University, Seoul 04107, South Korea (e-mail: suabae@sogang.ac.kr; tksong@sogang.ac.kr).

J. Park is with Samsung Electronics Co. Ltd., Suwon 18448, South Korea.

Digital Object Identifier 10.1109/TUFFC.2019.2931495

In [25], a row-column addressing matrix was suggested to transmit PWs with reduced TX hardware complexity. In this method, the PW angles form a cross pattern in the 2-D angular (lateral and elevational) space. Since the cross pattern yields a beam represented as a sum of two focused beams, one in the lateral direction and the other in the elevational direction, it generates high sidelobes in each direction [25]. In contrast, a fully 2-D angular pattern consisting of PW angles distributed on a square grid [2] enables dynamic TX focusing in every direction. However, the number of PW angles on a square grid increases to N^2, where N is the number of PW angles for a 1-D array with the same width.

In PWI with 1-D arrays, the distribution of the PW angles used for compounding regulates the main lobe width and the grating lobe positions in the beam pattern. As the range of PW angles increases, the main lobe width gets narrower, resulting in a better spatial resolution [26], [27]. In PWI, grating lobes are not only caused by regularly spaced transducer elements but also generated when a constant PW angular interval is employed [26]–[29]. As the constant angular interval increases, the grating lobes move closer to the main lobe, compromising the contrast resolution. Therefore, in PWI with a 2-D array, when the PW angles are distributed on a square grid, both the range and the number of PW angles should be sufficiently large to obtain high spatial and contrast resolutions. In this case, however, hundreds or thousands of PWs must be transmitted. Hence, the image quality may be compromised for ultrafast 3-D imaging [2].

The aim of this study is to reduce the number of PW angles for a given 2-D angular range while mitigating the grating lobe level, which will be accomplished by using PW angles that are distributed on aperiodic grids but have a rather uniform density. For this purpose, we propose two aperiodic angle patterns for 3-D PW synthetic focusing (PWSF): 1) a concentric ring pattern in which the PW angles are distributed with a uniform circular interval (i.e., constant arc length) on each set of concentric rings with uniform increments in the radial distance and 2) a sunflower pattern, which is a Fermat's spiral with a golden angle.

This article is organized as follows. In Section II, we formulate the theoretical (monochromatic) beam pattern of 3-D PWSF using a matrix array and show that the periodicity of PW angles causes grating lobes in 3-D PWSF. In Section III, two aperiodic angle sets (a concentric ring pattern and a sunflower pattern) are proposed to reduce the grating lobe level, and the beamforming and compounding schemes using these angle sets are also presented. In Section IV, the proposed methods are evaluated by analyzing beam patterns and simulated 3-D images. In Sections V and VI, the discussion and conclusions are presented.

II. Theory

A. Beam Pattern of 3-D PWSF Using a Continuous Angle

Fig. 1 illustrates the propagation of 2-D PWs fired from a 2-D rectangular array of size $D_x \times D_y$ located on the xy plane. At $t = 0$, each 2-D PW is centered at the original point (0, 0, 0), and its planar wavefront lies on the flat surface, for which

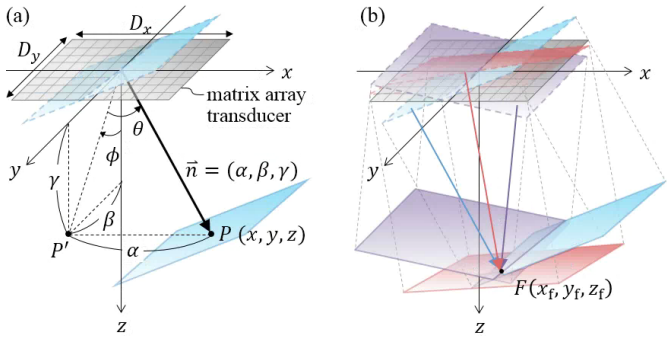

Fig. 1. (a) Normal vector $\vec{n}(\alpha, \beta, \gamma)$ of a 2-D PW. Point P' is the orthogonal projection of point P onto the yz plane. (b) Synthesis of multiple PWs at a focus $F(x_f, y_f, z_f)$.

the plane equation is expressed as follows:

$$x\alpha + y\beta + z\gamma = 0. \tag{1}$$

In Fig. 1(a), a 2-D PW traveling along the bold arrow reaches a point $P(x, y, z)$. Let us represent the direction of the arrow (or the point P) with the azimuth angle θ and the elevational angle ϕ. Then, the normal vector of the 2-D PW is denoted $\vec{n} = (\alpha, \beta, \gamma)$, where $\alpha = \sin\theta$ and $\beta = \cos\theta \sin\phi$. Note that the direction of a 2-D PW can be represented by only (α, β) since $\gamma = (1 - \alpha^2 - \beta^2)^{1/2}$. The time when the PW arrives at the point P is then defined as $t = (\alpha x + \beta y + \gamma z)/c$, where c is the speed of sound.

Let us assume that the planar wavefront is collimated within a certain volume due to the limited aperture ($D_x \times D_y$), such as with the PW transmitted by a 1-D array [30]. Within this volume, the acoustic field of a monochromatic 2-D PW with a normal vector $\vec{n} = (\alpha, \beta, \gamma)$ is given by

$$\Phi(x, y, z, t) = \Psi_{\alpha,\beta}(x, y, z)e^{j2\pi f_0 t} \tag{2}$$

where f_0 is the frequency of the PW. In the above equation, the spatial beam pattern $\Psi_{\alpha,\beta}(x, y, z)$ is expressed as follows:

$$\Psi_{\alpha,\beta}(x, y, z) = e^{-jk(\alpha x + \beta y + \gamma z)} \tag{3}$$

where k is the wavenumber ($k = 2\pi/\lambda$) and λ is the wavelength of the PW ($\lambda = c/f_0$).

Three-dimensional PWSF is conducted by compounding PWs propagating in different directions with synthetic TX delays to place them at a focal point $F(x_f, y_f, z_f)$ with the same phase, as shown in Fig. 1(b). Assuming that the angle of the PW, (α, β), varies continuously, the synthesized 3-D TX beam pattern can be described as follows:

$$\Psi(x, y, z) = \int_{-\infty}^{\infty}\int_{-\infty}^{\infty} p_s(\alpha, \beta)\Psi_{\alpha,\beta}(x, y, z)e^{jk\tau_{tx}(\alpha,\beta)}d\alpha\, d\beta \tag{4}$$

where $\tau_{tx}(\alpha, \beta)$ is the synthetic TX delay. $p_s(\alpha, \beta)$ is a synthetic window that confines an angular range of PWs to be compounded, where p_s can represent any shape of a finite angular range on the $\alpha\beta$ plane. By defining the synthetic TX delay as

$$\tau_{tx}(\alpha, \beta) = (\alpha x_f + \beta y_f + \gamma z_f)/c \tag{5}$$

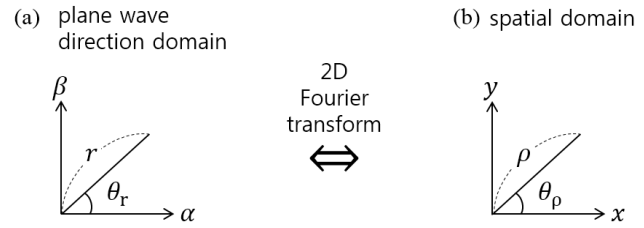

Fig. 2. (a) Cartesian (α, β) and polar (r, θ_r) coordinates in the PW direction domain. (b) Cartesian (x, y) and polar (ρ, θ_ρ) coordinates in the spatial domain.

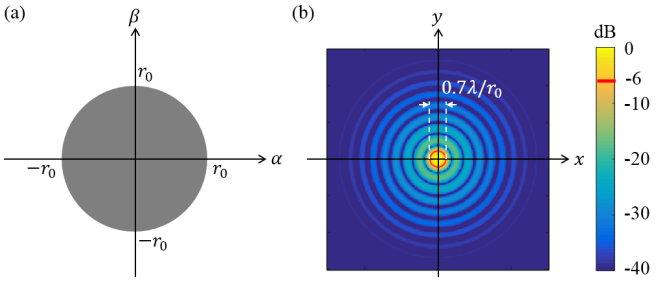

Fig. 3. (a) Synthetic window p_s, which represents an infinite number of PWs with a propagation direction of $(\alpha^2 + \beta^2)^{1/2} < r_0$ and (b) 2-D synthetic TX beam pattern using the continuous PW angles presented in (a). The −6-dB beamwidth (W_B) of the beam pattern is $0.7\lambda/r_0$.

and substituting (3) and (5) into (4), the 2-D beam pattern on the xy plane at the focal depth ($z = z_f$) reduces to

$$\Psi(x', y') = \int_{-\infty}^{\infty}\int_{-\infty}^{\infty} p_s(\alpha, \beta) e^{-jk(\alpha x' + \beta y')} d\alpha\, d\beta = P_s(x'/\lambda, y'/\lambda) \tag{6}$$

where $x'(= x - x_f)$ and $y'(= y - y_f)$ are the translated coordinates centered at (x_f, y_f) and $P_s(\cdot)$ is the 2-D Fourier transform of $p_s(\cdot)$. For the convenience of analysis, the angular range defined by p_s is circularly symmetric in this article.

Let (r, θ_r) and (ρ, θ_ρ) denote the polar coordinates to represent the PW direction in the $\alpha\beta$ plane and a point in the xyplane, respectively, as illustrated in Fig. 2. If PWs with a range of PW directions of $r < r_0$ are employed, as shown in Fig. 3(a), then p_s is expressed by a circularly symmetric function

$$p_s(r) = \mathrm{circ}(r/r_0) = \begin{cases} 1, & r < r_0 \\ 1/2, & r = r_0 \\ 0, & r > r_0. \end{cases} \tag{7}$$

Substituting (7) into (6) gives the closed-form expression of the PWSF beam pattern, which is also circularly symmetric (see Appendix A)

$$\Psi_{\mathrm{cont.}}(\rho) = \pi r_0^2 \mathrm{jinc}(2r_0\rho/\lambda) \tag{8}$$

since the Fourier transform of a disk function is a jinc function. The result is plotted in Fig. 3(b). Since the full-width half-maximum (FWHM) of the main lobe of the jinc function, $\mathrm{jinc}(R\rho)$, is approximately $1.4/R$, the FWHM beamwidth (W_B) of the synthetic beam pattern in (8) is given by

$$W_B \approx 1.4\lambda/(2r_0) = 0.7\lambda/r_0. \tag{9}$$

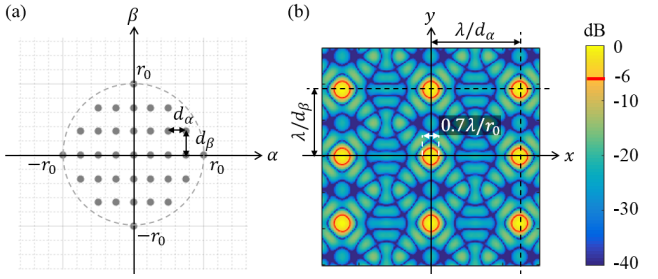

Fig. 4. (a) PW set of periodic patterns with a range of r_0. Each seed (gray dot) represents a PW with a direction of (α_n, β_n), where $n = 0, 1, \ldots, N-1$. (b) 2-D synthetic TX beam pattern using the PWs presented in (a). The −6-dB beamwidth (W_B) of the beam pattern is $0.7\lambda/r_0$ and the grating lobes arise at intervals of λ/d_α and λ/d_β in the x- and y-directions, respectively.

B. Beam Pattern of PWSF Using Discrete Angles

In practice, the PW directions must be discretized. When N PWs are used for the PWSF, the synthetic window can be represented by a sum of Dirac delta functions as follows:

$$p_s(\alpha, \beta) = \sum_{(\alpha_n, \beta_n) \in \mathbb{S}} \delta(\alpha - \alpha_n, \beta - \beta_n) \tag{10}$$

where $\mathbb{S} = \{(\alpha_0, \beta_0), (\alpha_1, \beta_1), \ldots, (\alpha_{N-1}, \beta_{N-1})\}$ denotes a set of PW directions and each element of $\mathbb{S}$ will be called a seed. By using the synthetic window that represents the distribution of PW angles, the beam pattern is obtained by substituting (10) into (6) as follows:

$$\Psi(x\prime, y\prime) = \sum_{(\alpha_n, \beta_n) \in \mathbb{S}} e^{-jk(\alpha_n x' + \beta_n y')}. \tag{11}$$

C. PW Set of Periodic Pattern

Let us first consider the case in which N seeds in (10) are distributed periodically on a rectangular grid, as shown in Fig. 4(a). Then, the synthetic window can be defined as follows:

$$p_s(\alpha, \beta) = \mathrm{circ}\left(\frac{r}{r_0}\right) \cdot \sum_{p=-\infty}^{\infty}\sum_{q=-\infty}^{\infty} \delta(\alpha - d_\alpha p, \beta - d_\beta q) \tag{12}$$

where d_α and d_β are the intervals of the N seeds in α and β, respectively. Since the synthetic beam pattern is expressed as the Fourier transform of the synthetic window (p_s), the beam pattern for the synthetic window in (12) is the convolution of the Fourier transforms of the two factors on the right-hand side of (12), which is expressed as follows:

$$\Psi_{\mathrm{PD}} = \pi r_0^2 \mathrm{jinc}(2r_0\rho/\lambda) * \sum_{p=-\infty}^{\infty}\sum_{q=-\infty}^{\infty} \delta\left(x' - \frac{\lambda}{d_\alpha}p, y' - \frac{\lambda}{d_\beta}q\right). \tag{13}$$

Fig. 4(b) shows that the resultant 2-D beam profile has the main lobe at the center ($x = 0$, $y = 0$), which is identical to the beam pattern of (8) for the continuous synthetic window. In PW imaging with a 1-D array, the PW angle varies only in the α direction, and hence grating lobes are observed along the x-axis [27]. Since the PW angles are periodically sampled in both the α and β directions in Fig. 4(a), the resultant beam

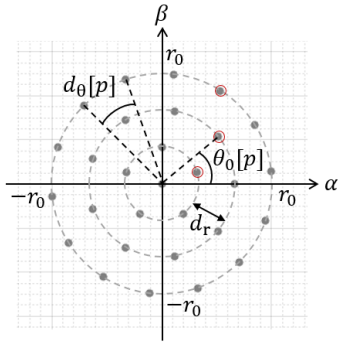

Fig. 5. PW set of concentric ring patterns with a range of r_0. The rings have different radii with an interval of d_r, and the seeds on the pth ring are regularly distributed with an angular interval of $d_\theta[p]$. The first seed in each ring is indicated by a red circle, and its angle is denoted by $\theta_0[p]$.

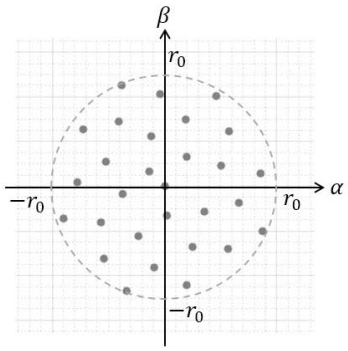

Fig. 6. PW set of the sunflower pattern with a range of r_0.

pattern would exhibit grating lobes at integer multiples of λ/d_α and λ/d_β in the x- and y-directions, respectively, as shown in Fig. 4(b).

The round-trip beam pattern is the product of the TX beam pattern and the receive beam pattern. The magnitude of the grating lobes in Fig. 4(b) is reduced after being multiplied by the focused receive beam pattern. Note that both d_α and d_β should be sufficiently small to move the grating lobes farther from the main lobe (focus), and thereby to suppress them below the level required in B-mode imaging. However, to achieve a high volume rate, the number of PWs should be reduced by increasing d_α and d_β. Then, the grating lobes will move closer to the main lobe, and hence degrade the image quality.

III. Methods

A. Aperiodic PW Angle Distributions

From the grating lobe artifact point of view, using the periodic PW set is not an optimal strategy. In this article, we propose two aperiodic direction patterns that yield improved beam patterns with fewer PWs (i.e., using a smaller number of seeds).

1) PW Set of Concentric Ring Pattern: Concentric rings with a constant radial interval can provide a uniform spatial density of seeds in polar coordinates while avoiding periodicity in the $\alpha\beta$ space [31]. The nth PW direction [i.e., (α, β) of the nth seed, $n = 0, 1, \ldots, N-1$] of a concentric ring pattern is defined as follows:

$$\begin{aligned} \alpha_n &= d_r p \cos(\theta_0[p] + d_\theta[p] \cdot q) \\ \beta_n &= d_r p \sin(\theta_0[p] + d_\theta[p] \cdot q) \\ p &= 0, 1, \cdots, P-1, q = 0, 1, \cdots, Q[p]-1 \end{aligned} \quad (14)$$

where $P-1$ is the number of concentric rings; $Q[p]$ is the number of seeds in the pth ring, with $Q[0] = 1$; d_r is the uniform radial interval between concentric rings; $d_\theta[p]$ is the angular interval between the seeds on the pth ring; and $\theta_0[p]$ is the angle of the first seed on the pth ring. An example of a concentric ring pattern is presented in Fig. 5.

For a given total number of PWs ($N = Q[0] + Q[1] + \ldots + Q[P-1]$), P and $Q[p]$ should be determined so that the arc length between two successive seeds on each ring is close to d_r in an effort to achieve a high degree of uniform density. In this article, P was chosen such that $N \approx 1 + \sum_{p=1}^{P-1} 2\pi p = \pi P^2 - \pi P + 1$ (see Appendix B). Different angles of the first seeds on each ring ($\theta_0[p]$) are selected to avoid periodicity by distributing the first-seed angles as $\theta_0[p] = d_\theta[p] \cdot p/P$. The first seeds are indicated by red circles in Fig. 5. The concentric ring pattern in Fig. 5 clearly shows that its seeds are not distributed on the periodic rectangular grid, as in Fig. 4(a), and so it would not produce the regularly placed grating lobes as shown in Fig. 4(b). In the concentric ring pattern, however, the seeds are not randomly distributed, and hence other specific grating lobes are still expected, whose pattern and levels will be investigated in Section IV.

2) PW Set of the Sunflower Pattern: Another set of uniformly distributed but aperiodic PW directions can be obtained from a Fermat's spiral with the golden angle, which is the so-called sunflower pattern [32]. This sunflower pattern was already demonstrated to effectively break the periodicity of the 2-D array elements of an US transducer or antenna in order to limit the grating lobe level in sparse array design [33]–[35]. The nth PW direction ($n = 0, 1, \ldots, N-1$) of the sunflower pattern is defined as follows:

$$\begin{aligned} \alpha_n &= r_0 \sqrt{n}/(N-1) \cos(n\theta_G) \\ \beta_n &= r_0 \sqrt{n}/(N-1) \sin(n\theta_G) \end{aligned} \quad (15)$$

where the golden angle θ_G is $\pi(\sqrt{5}-1)$. Fig. 6 presents an example of a sunflower pattern. No seeds have the same angular position, which results in reduced periodicity.

B. Beamforming for 3-D PWI

In the proposed 3-D US imaging using 2-D PW angle sets, each PW is fired consecutively, and the backscattered US waves are received at all array elements. Then, each imaging point is reconstructed by performing 3-D PWSF using the synthesis delays of (5) and receive dynamic focusing (RDF). Therefore, dynamic focusing is achieved on both transmission and reception. Such two-way dynamic focusing can provide high spatial and contrast resolutions over the entire field of view.

Due to the finite 2-D array size, each PW propagates through a confined region of the volume of interest as with a 1-D array transducer [30], [36]. For instance, when

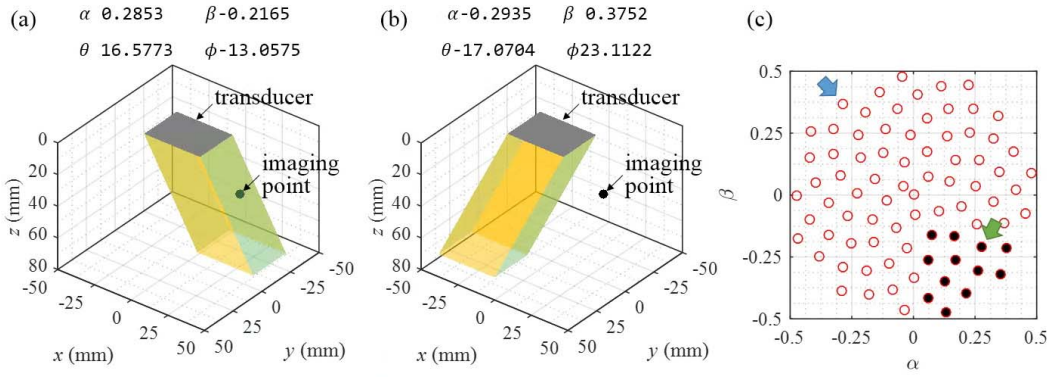

Fig. 7. (a) Propagating region (yellow volume) of a PW that reaches the imaging point at $\mathbf{x}_\mathrm{f}$ (20, −20, 40 mm). (b) Propagating region (yellow volume) of a PW that does not reach the imaging point. (c) Example of a direction pattern of total PWs (set $\mathbb{T}$, red circles) and PWs [subset $\mathbb{S}(\mathbf{x}_\mathrm{f})$, black dots] that reach the imaging point. The direction (α, β) and the angle (θ, ϕ) of each PW are presented on the top of panels (a) and (b). The (α,β) of the PWs of (a) and (b) are also indicated in (c) by green and blue arrows, respectively.

$D_x = 38.1$ mm and $D_y = 28.5$ mm, Fig. 7(a) illustrates a PW whose propagation region encompasses an imaging point $\mathbf{x}_\mathrm{f} = (20, -20, 40)$ mm, whereas Fig. 7(b) depicts another PW that does not reach the imaging point. In Fig. 7(c), only the seeds marked with black dots (denoting active seeds) represent the PWs that propagate through the imaging point when a golden-angle spiral pattern ($N = 88$, $r_0 = 0.5$) is employed. The seeds that represent the directions of the PWs of Fig. 7(a) and (b) are marked by green and blue arrows in Fig. 7(c), respectively.

Let $\mathbb{T} = \{(\alpha_0, \beta_0), (\alpha_1, \beta_1), \ldots, (\alpha_{N-1}, \beta_{N-1})\}$ denote a set of total PWs and $\mathbb{S}(\mathbf{x}_\mathrm{f})$ denote a subset of $\mathbb{T}$ that contains only the active seeds for $\mathbf{x}_\mathrm{f}$. Then, the beamformed signal at each imaging point $\mathbf{x}_\mathrm{f} = (x_\mathrm{f}, y_\mathrm{f}, z_\mathrm{f})$ can be expressed as follows:

$$g(\mathbf{x}_\mathrm{f}) = \frac{1}{N_s} \sum_{(\alpha_n, \beta_n) \in \mathbb{S}(\mathbf{x}_\mathrm{f})} \sum_{m=0}^{M-1} w_\mathrm{rx}[m] r_{n,m}(\tau^{n,m}) e^{-j\omega_0 \tau^{n,m}} \tag{16}$$

where $r_{n,m}$ represents the complex base-band signal received by the mth element for the nth PW and w_rx is a receive apodization function. The N_s is the number of angles in the $\mathbb{S}(\mathbf{x}_\mathrm{f})$. The term $e^{-j\omega_0 \tau^{n,m}}$ is a phase rotation term generally used for base-band beamforming, where ω_0 is the angular frequency of the PW. In (16), $\tau^{n,m}$ is the beamforming delay that consists of delays for PWSF and RDF, that is,

$$\tau^{n,m} = \left(\alpha_n x_\mathrm{f} + \beta_n y_\mathrm{f} + \sqrt{1 - \alpha_n^2 - \beta_n^2} z_\mathrm{f}\right)/c + \left(\sqrt{\left(x_\mathrm{f} - x_\mathrm{e}^m\right)^2 + \left(y_\mathrm{f} - y_\mathrm{e}^m\right)^2 + \left(z_\mathrm{f} - z_\mathrm{e}^m\right)^2}\right)/c \tag{17}$$

where $(x_\mathrm{e}^m, y_\mathrm{e}^m, z_\mathrm{e}^m)$ is the position of the mth transducer element.

C. Beam Pattern Analysis

For the comparison of the 3-D PWSFs using the three PW sets (periodic, concentric ring, and sunflower), their TX beam patterns in the xy plane at $z = z_\mathrm{f}$ were investigated by evaluating (11). Since the fundamental property of the field response of a beamforming scheme is better understood with monochromatic excitation, all the TX beam patterns were obtained for the case where a continuous wave (CW) with a center frequency of 3 MHz was transmitted from a rectangular transducer of size 38.4 mm (D_x)× 28.8 mm (D_y). The sound speed was assumed to be 1540 m/s.

Three angle sets ($\mathbb{T}_\mathrm{p}$ for the periodic rectangular grid, $\mathbb{T}_\mathrm{c}$ for the concentric ring, and $\mathbb{T}_\mathrm{s}$ for the sunflower) were determined according to (12), (14), and (15), and each set has N seeds (i.e., N PWs), where $r < r_0 = 0.5$ ($r = (\alpha^2 + \beta^2)^{1/2}$). The number of PWs, N, was 81, 149, or 253. The TX beam patterns were obtained for the three focal points $\mathbf{x}_\mathrm{f}^1 = (0, 0, 20)$, $\mathbf{x}_\mathrm{f}^2 = (0, 0, 50)$, and $\mathbf{x}_\mathrm{f}^3 = (20, -20, 40)$, where all dimensions are in millimeters (mm).

As described in Section III-B, the active seeds (PWs that reach each focal point) vary with the focal point. Therefore, different subsets of each $\mathbb{T}_\mathrm{p}$, $\mathbb{T}_\mathrm{c}$, and $\mathbb{T}_\mathrm{s}$ are selected for the three focal points, which are defined as $\mathbb{S}_\mathrm{p}(\mathbf{x}_\mathrm{f}^k)$, $\mathbb{S}_\mathrm{c}(\mathbf{x}_\mathrm{f}^k)$, and $\mathbb{S}_\mathrm{s}(\mathbf{x}_\mathrm{f}^k)$ for $k = 1, 2, 3$. Each beam pattern is obtained by compounding the PWs contained in each subset $\mathbb{S}$.

Theoretically, the active seeds of the periodic PW set produce grating lobes with a regular interval λ/d in both the x- and y-directions, as described in Section II-C. However, the grating lobe intervals for PW sets with an aperiodic angle distribution cannot be determined theoretically. In the beam pattern of the aperiodic PW set, we found a distinct grating lobe ring, which will be presented in Section IV-A5. Here, we adopt a Delaunay triangulation-based analysis, which was suggested previously in [37], to obtain the theoretical position of the first grating lobe ring. We compared the theoretical grating lobe position and the position measured from the beam pattern for each of the three PW sets.

D. Evaluation of 3-D Images

Pulsed-wave beam simulations were conducted to obtain the 3-D PWSF images of two hypothetical phantoms that consist of two different sets of point scatterers by using the periodic, concentric ring, and sunflower PW sets. The first

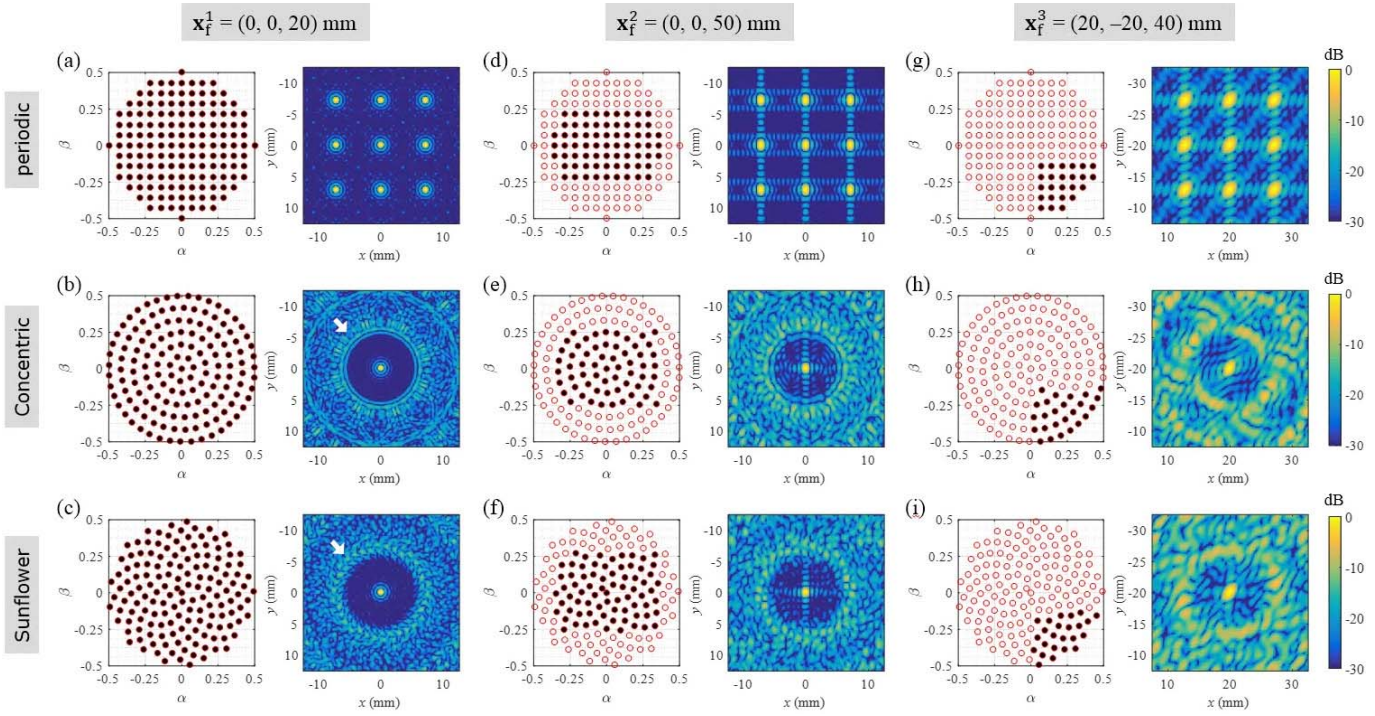

Fig. 8. PW direction sets $\mathbb{T}$ ($N = 149$) and subsets $\mathbb{S}$ (left) and synthetic TX beam patterns (right) for the focal points at (a)–(c) $\mathbf{x}_f^1 = (0, 0, 20)$ mm, (d)–(f) $\mathbf{x}_f^2 = (0, 0, 50)$ mm, and (g)–(i) $\mathbf{x}_f^3 = (20, -20, 40)$ mm when using (a), (d), and (g) periodic, (b), (e), and (h) concentric ring, and (c), (f), and (i) sunflower PW angle patterns. In the left, the seeds of direction set $\mathbb{T}$ and subset $\mathbb{S}$ are indicated by red circles and black dots, respectively. The PWs of each subset are employed for each synthetic beam pattern.

hypothetical phantom consists of seven point scatterers with a regular interval of 10 mm from $z = 10$ mm to $z = 70$ mm along the center scanline ($x = y = 0$), and the second phantom has two columns of seven scatterers along two scanlines. The steering angles of the two scanlines are ($\theta = 30°$, $\phi = 0°$) and ($\theta = 0°$, $\phi = 23.4°$); each scanline lies on the xz plane or yz plane.

In these computer experiments, a 128 × 96-element matrix transducer was used. The central frequency of the transducer was assumed to be 3 MHz and the pitch was 0.3 mm [i.e., the size of the transducer was 38.4 mm (D_x)× 28.8 mm (D_y)]. The fractional bandwidth of the transducer was set to 78.7%. To transmit a PW, a single US pulse with a central frequency of 3 MHz was used, and no TX apodization window was applied. Radio-frequency (RF) data were obtained at 12 MHz using Field II [38]. A 3-D volume with a trapezoidal prism shape was reconstructed by employing STF and RDF for each imaging point according to (16). The 50% Tukey window was applied for receive dynamic apodization (w_{rx}) with an F-number of 1.

To assess the proposed methods, the spatial resolution and contrast of the point spread function (PSF) of each method were measured. The spatial resolution and contrast were measured as a function of the imaging depth and the number of transmitted PWs (N). A point target was placed at a certain position at which the resolution or contrast was measured. A PSF was obtained by reconstructing a 3-D beamformed image of the point target according to (16). For the spatial resolution, the FWHM of the main lobe of each 3-D PWSF method was measured from its PSF in the lateral (in the xz plane) and elevational (in the yz plane) directions. The contrast was defined as follows:

$$\mathrm{contrast(dB)} = -10\log_{10}\left(\frac{\iiint_{\mathbf{x}\notin S}|g(\mathbf{x})|^2 d\mathbf{x}}{\iiint|g(\mathbf{x})|^2 d\mathbf{x}}\right) \tag{18}$$

where $g(\mathbf{x})$ is the PSF image and S is a small sphere with a radius of 5λ centered at the point target [39]. The numerator is the power of the sidelobe and grating lobe artifacts, and the denominator is the total power of the PSF image. The negative sign makes the higher values of (18) represent better image contrasts.

IV. Results

A. Beam Pattern Analysis

1) PW Sets and Active Seeds: Fig. 8 shows three PW sets ($\mathbb{T}_{\mathrm{p}}$, $\mathbb{T}_{\mathrm{c}}$, and $\mathbb{T}_{\mathrm{s}}$, $N = 149$) whose elements (i.e., PW directions) are represented by red circles on the left panel of each subfigure [Fig. 8(a)–(i)], and the subsets $\mathbb{S}$ for each focal point are marked with black dots. Shown to the right of each subfigure is the corresponding CW TX beam pattern. For the first focal point $\mathbf{x}_f^1$, which is located at a shallow depth ($z = 20$ mm) on the center scanline (on the z-axis), all the PWs with directions defined by $\mathbb{T}_{\mathrm{p}}$, $\mathbb{T}_{\mathrm{c}}$, and $\mathbb{T}_{\mathrm{s}}$ reach the point. Therefore, the subset $\mathbb{S}$ is identical to $\mathbb{T}$, that is, $\mathbb{S}_{\mathrm{p}}(\mathbf{x}_f^1) = \mathbb{T}_{\mathrm{p}}$, $\mathbb{S}_{\mathrm{c}}(\mathbf{x}_f^1) = \mathbb{T}_{\mathrm{c}}$, and $\mathbb{S}_{\mathrm{s}}(\mathbf{x}_f^1) = \mathbb{T}_{\mathrm{s}}$, as shown in Fig. 8(a)–(c).

In the case of $\mathbf{x}_f^2$, the focal depth is moved further on the z-axis, and the active seeds (elements of subset $\mathbb{S}$) are confined in the center area in the $\alpha\beta$ plane, as shown in Fig. 8(d)–(f),

because the PWs with large steering angles do not propagate over $\mathbf{x}_f^2$. Note that the active seeds are distributed over a larger area along the αdirection in all PW patterns, which is an expected result because the rectangular transducer used has a larger width in this direction.

The third focal point $\mathbf{x}_f^3$ is off the z-axis by 20 and -20 mm along the x- and y-directions, respectively. Therefore, the active seeds $\mathbb{S}$ in each PW set are confined to the bottom-right corner ($\alpha > 0$ and $\beta < 0$) of each $\mathbb{T}$ space, as shown in the left panels of Fig. 8(g)–(i).

In the cases of $\mathbf{x}_f^2$ and $\mathbf{x}_f^3$, the numbers of active seeds of the three patterns are different because the discretized angles are obtained with different sampling geometries (patterns).

2) Main Lobe Patterns: Fig. 8 shows that the main lobe is centered on the targeted focal point in all cases. The main lobes of the PWSFs using periodic, concentric ring, and sunflower sets are circularly symmetric [see Fig. 8(a)–(c)] with -6-dB beamwidths of 0.73, 0.67, and 0.72 mm, respectively. The reason why the concentric ring provides a slightly smaller beamwidth is that it has as many seeds as possible at the boundary (outer ring at $r = r_0 = 0.5$). In contrast, the periodic and sunflower PW sets have much smaller numbers of seeds on the boundary. Hence, the concentric ring PW set ($\mathbb{T}_c$) has the largest effective range of PW angles.

In Fig. 8(d)–(f), for $\mathbf{x}_f^2$, the main lobes for all PW sets have asymmetric shapes that resemble ellipses whose major axis is the y-axis, which is also an expected result because the range of active seeds is larger in the α direction than in the β direction. Compared to the case of $\mathbf{x}_f^1$, the active seeds of all PW sets for $\mathbf{x}_f^2$ are confined in smaller areas, which leads to larger -6-dB beamwidths. For example, the -6-dB beamwidths for the periodic, concentric ring, and sunflower PW sets [$\mathbb{S}_p(\mathbf{x}_f^2)$, $\mathbb{S}_c(\mathbf{x}_f^2)$, and $\mathbb{S}_s(\mathbf{x}_f^2)$] are 0.87, 0.89, and 0.87 mm along the x-axis, respectively, and 1.3, 1.2, and 1.2 mm along the y-axis, respectively.

Finally, Fig. 8(g)–(i) shows that the main lobes for $\mathbb{S}_p(\mathbf{x}_f^3)$, $\mathbb{S}_c(\mathbf{x}_f^3)$, and $\mathbb{S}_s(\mathbf{x}_f^3)$ are tilted along the diagonal direction in the xy plane because the active seeds are located only in the fourth quadrant of the $\alpha\beta$ plane. Since the 2-D ranges of the active seeds for $\mathbf{x}_f^3$ are reduced compared to those for $\mathbf{x}_f^2$, the main lobes have increased beamwidths, as observed clearly in Fig. 8(g)–(i). The -6 dB beamwidths of the beam patterns at $\mathbf{x}_f^3$ using the periodic, concentric ring, and sunflower PW sets are 1.6, 1.3, and 1.5 mm along the x-axis, respectively, and 1.9, 1.7, and 1.8 mm along the y-axis, respectively.

The above results indicate that the main lobe characteristic of the 3-D PWSF is not influenced by the geometry of the angle distribution. For the same focal point, the main lobe patterns of the three PW sets are slightly different only in terms of the beamwidth because the ranges of active seeds for the three PW sets cannot be equal due to different geometries of the sampling (discretizing) PW angles.

3) Grating and Sidelobe Patterns: Compared with the main lobe, the grating lobes of the three PW sets exhibit different patterns. The influence of the sampling geometry on the grating lobes can be best investigated when $\mathbb{T} = \mathbb{S}$, as in Fig. 8(a)–(c). The periodic PW set produces grating lobes with the same peak magnitude as that of the main lobe, and they are also periodically distributed on a rectangular grid in the xy plane, as shown in the right panel of Fig. 8(a).

TABLE I

PEAK MAGNITUDES OF THE GRATING LOBES OF THE BEAM PATTERNS OF THE PERIODIC, CONCENTRIC RING, AND SUNFLOWER SETS WHEN $N = 149$

Imaging point (mm)	Peak magnitude of grating lobes (dB)		
	Periodic	Concentric ring	Sunflower
$\mathbf{x}_f^1$ (0, 0, 20)	0	–11.4	–11.4
$\mathbf{x}_f^2$ (0, 0, 50)	0	–8.6	–7.2
$\mathbf{x}_f^3$ (20, –20, 40)	0	–3.9	–4.6

In the case of the concentric ring [Fig. 8(b)], a circular symmetric grating lobe pattern is observed, which is the expected result due to the circular symmetric distribution of the active seeds. The first grating lobe is clearly visible as a distinct ring indicated by a white arrow (with a radius of approximately 7.3 mm), which has a smaller value than the main lobe peak (-11.4 dB). Moreover, the second grating lobe appears on an outer ring with a radius of approximately 14.5 mm, and it also has a smaller magnitude (-11.3 dB). Between the first and second rings of the grating lobe, the sidelobe levels are elevated to at most -13.9 dB.

The sunflower PW set [Fig. 8(c)] $\mathbb{T}_s$ exhibits a grating lobe pattern (indicated by a white arrow) and a sidelobe pattern similar to those of the concentric PW set, although the first grating lobe pattern does not appear as a distinct ring. This finding implies that $\mathbb{T}_s$ has aperiodic sampling geometries in both the α and β directions as with $\mathbb{T}_c$, and it may also be stated that $\mathbb{T}_s$ has a circular symmetric nature in a sense.

Fig. 8(d) and (g) reveals that the sidelobe levels increase as the number of active seeds decreases. Fig. 8(e) shows that the ring of the grating lobe is not as distinctive as in Fig. 8(b) because the active seeds shown in Fig. 8(e) became less circularly symmetrical and the number of active seeds is considerably reduced compared to that in Fig. 8(b). Similar results are observed in Fig. 8(f).

Note that the active seeds of $\mathbb{S}_c(\mathbf{x}_f^2)$ and $\mathbb{S}_s(\mathbf{x}_f^2)$ are located within a rectangular region due to the shape of the transducer used, which could cause a loss of the circular symmetry of the seed distribution to some degree. As a result, the sidelobe levels inside the first grating lobe ring in Fig. 8(e) and (f) are elevated compared to those in Fig. 8(b) and (c), forming cross patterns. If a circular transducer can be employed, the cross-shaped sidelobe might be reduced.

The total number of active seeds of each PW set for $\mathbf{x}_f^3$ are all reduced greatly, as shown in the left panels of Fig. 8(g)–(i). Moreover, the concentric ring and sunflower patterns are no longer maintained in $\mathbb{S}_c(\mathbf{x}_f^3)$ and $\mathbb{S}_s(\mathbf{x}_f^3)$. Consequently, the grating lobe ring patterns are barely visible in the right panels of Fig. 8(h) and (i).

Table I presents the peak grating lobe magnitudes of all the beam patterns of the three PW sets in Fig. 8. The peak magnitude of the first grating lobe ring was measured for the aperiodic cases. Table I indicates that the two aperiodic PW

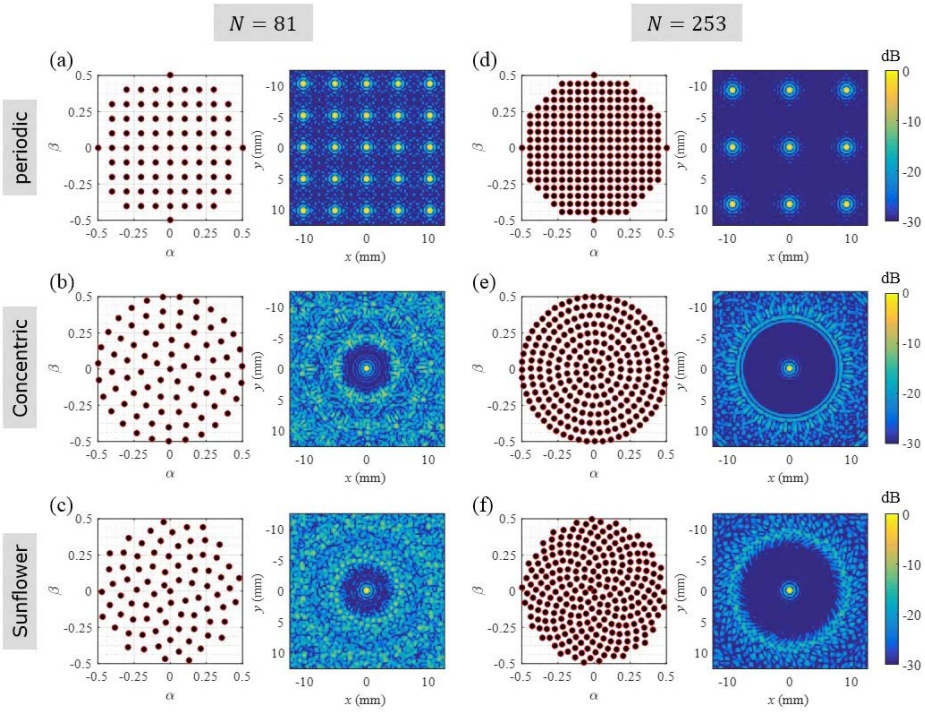

Fig. 9. PW direction sets $\mathbb{T}$ (a)–(c) $N = 81$ or (d)–(f) $N = 253$ and subsets $\mathbb{S}$ (left) and synthetic TX beam patterns (right) for the focal points at $\mathbf{x}_{\mathrm{f}}^1 = (0, 0, 20)$ mm when using the (a) and (d) periodic, (b) and (e) concentric ring, and (c) and (f) sunflower patterns. In the left, the seeds of set $\mathbb{T}$ (red circles) are equal to the seeds of subset $\mathbb{S}$ (black dots). All PWs in $\mathbb{T}$ are employed for each synthetic beam pattern.

sets contribute to suppressing the grating lobes by 11.4 dB for the focal point $\mathbf{x}_{\mathrm{f}}^1$. For $\mathbf{x}_{\mathrm{f}}^2$, the grating lobe suppression level decreases to 8.6 and 7.2 dB when using the concentric ring and sunflower PW sets, respectively. For $\mathbf{x}_{\mathrm{f}}^3$, the grating lobe reduction is reduced to 3.9 and 4.6 dB with $\mathbb{S}_{\mathrm{c}}(\mathbf{x}_{\mathrm{f}}^3)$ and $\mathbb{S}_{\mathrm{s}}(\mathbf{x}_{\mathrm{f}}^3)$, respectively, because of the loss of distinctive patterns due to the small number of active elements.

4) Effects of the Number of Seeds (PWs) on the Beam Pattern: Fig. 9 shows the CW TX beam patterns for $\mathbf{x}_{\mathrm{f}}^1$ for the three PW sets used in Fig. 8 when $N = 81$ and 253. Fig. 9(a)–(c) ($N = 81$), Fig. 8(a)–(c) ($N = 149$), and Fig. 9(d)–(f) ($N = 253$) show that the main lobe width does not change with N as long as the angular range of each set remains the same. However, one can clearly see that the properties of the sidelobes and grating lobes vary significantly with the value of N. For all PW sets, one can also see that the radius of the ring increases and that the sidelobe levels are lowered with increasing N, from $N = 81$ [Fig. 9(a)–(c)] to $N = 149$ [Fig. 8(a)–(c)] and to $N = 253$ [Fig. 9(d)–(f)]. Note that the ring patterns of the grating lobes in Fig. 9(b) and (c) are blurred and not as clearly visible as in Fig. 8(b) and (c). In contrast, when N increases to 253 [Fig. 9(e) and (f)], the grating lobes form a ring pattern more distinctively than those in Fig. 8(b) and (c).

5) Theoretical Radius of Grating Lobe Ring of Aperiodic PW Sets: Fig. 10(a) and (b) shows Delaunay triangulations of the seeds of the concentric ring and sunflower patterns, respectively, when $N = 149$; the length of the line segments represents the distance between neighboring seeds. The

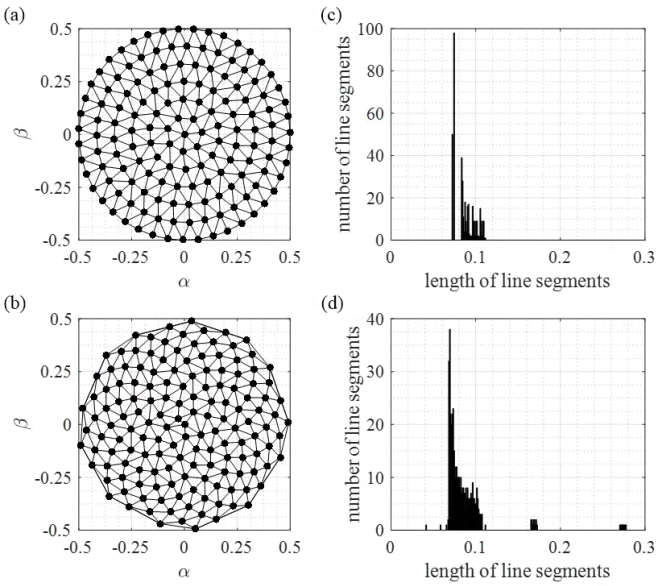

Fig. 10. (a) and (b) Delaunay triangulation of seeds ($N = 149$) of the (a) concentric ring pattern and (b) sunflower pattern used in Fig. 8(b) and (c), respectively. The length of the line segment presents the distance between neighboring seeds. (c) and (d) Histogram of the lengths of the line segments in (a) and (b), respectively. The most likely values of the length, $\hat{d}$, in (c) and (d) are 0.0745 and 0.0695, respectively.

histogram of the lengths of the triangulation line segments for each PW set is shown in Fig. 10(c) and (d). The most likely interval, $\hat{d}$, is then the line segment length at which the histogram has a peak value [37], which is 0.0745 and

TABLE II

THEORETICAL (λ/d_α) AND MEASURED LATERAL POSITIONS OF THE GRATING LOBES OF THE PERIODIC PW SET AND THEORETICAL ($\lambda/\hat{d}$) AND MEASURED RADII OF THE GRATING LOBE RING OF THE APERIODIC PW SETS WHEN FIOCUSING AT $\mathbf{x}_F^1$(0, 0, 20 MM)

N	lateral position of GL of the periodic set (mm)		radius of GL of the concentric ring set (mm)		radius of GL of the sunflower set (mm)	
	theoretical (λ/d_α)	measured	theoretical ($\lambda/\hat{d}$)	measured	theoretical ($\lambda/\hat{d}$)	measured
81	5.13	5.13	4.41	5.03	5.43	5.42
149	7.19	7.19	6.89	6.95	7.39	7.31
253	9.24	9.24	9.09	8.53	9.78	9.34

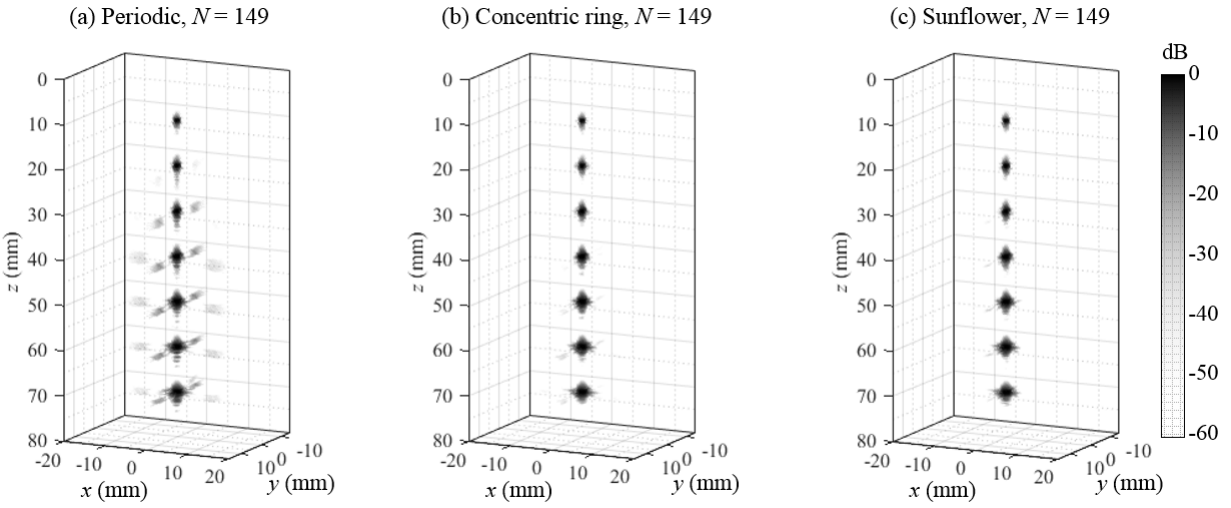

Fig. 11. 3-D images of seven-point targets at the center scanline reconstructed by using the (a) periodic, (b) concentric ring, and (c) sunflower PW patterns. The point targets are located at depths of 10, 20, 30, 40, 50, 60, and 70 mm.

0.0695 in Fig. 10(c) and (d), respectively. We will assume that the theoretical radius of the first grating lobe ring is approximately given by $\lambda/\hat{d}$.

The theoretical and the measured grating lobe positions by the three PW sets for the focal point $\mathbf{x}_f^1$ when $N = 81$, 149, and 253 are listed in Table II. The theoretical positions were obtained by using λ/d and $\lambda/\hat{d}$ for the periodic and aperiodic cases, respectively. The measured positions were obtained from the beam patterns in Figs. 8(a)–(c) and 9. In the aperiodic cases, measuring the radius of the grating lobe ring is difficult because the energy of the ring is scattered and does not form a single lobe. Thus, we transformed the beam pattern into polar coordinates (ρ, θ_ρ), accumulated the magnitude of the beam pattern over θ_ρ from 0° to 360°, and smoothed it with a moving average filter (Hanning window, length = 2.5 mm) along the ρ-axis. The measured grating lobe position (i.e., the radius of the ring) was determined as the ρ value at which the smoothed radial beam pattern has a peak value outside the main lobe region.

For the periodic PW set, the measured values match the theoretical grating lobe intervals perfectly at all depths. When the sunflower PW set is used, the measured values are consistent with the theoretical values. For the concentric ring set, though small differences are observed between the theoretical and measured values, they both increase with N and are observed to be closely related.

Table II also indicates that the radius of the first grating lobe of the sunflower set is always larger than the grating lobe position of the periodic set. In addition, as already seen in Fig. 8 and Table I, the sunflower set produces 11.4 dB lower grating lobes than that of the periodic set at $z = 20$ mm. Hence, the sunflower set is superior to the periodic set with regard to the grating lobe. The concentric ring produces a ring of grating lobes that is slightly closer to the main lobe for all values of N compared to the sunflower. This result may occur because the concentric ring pattern has a less dense distribution of seeds than the sunflower because the concentric ring pattern was designed to have more seeds at the boundary of $r = 0.5$.

B. Evaluation of 3-D Images

1) 3-D and Cross-Sectional Images: Fig. 11 shows the 3-D images of the first hypothetical phantom for the (a) periodic, (b) concentric ring, and (c) sunflower PW sets when $N = 149$; the dynamic range was set to 60 dB. Fig. 11(a) shows that the periodic PW set produces grating lobes (> -60 dB). Notably, when the concentric ring or sunflower PW set is used, the grating lobe artifacts are suppressed below -60 dB and do not appear in Fig. 11(b) and (c).

Fig. 12 presents cross-sectional images of each of the 3-D images in Fig. 11, which are obtained in the xz plane at $y = 0$, in the yz plane at $x = 0$, and in the xy plane at $z = 40$ mm from top to bottom. In Fig. 12, we increased the dynamic range

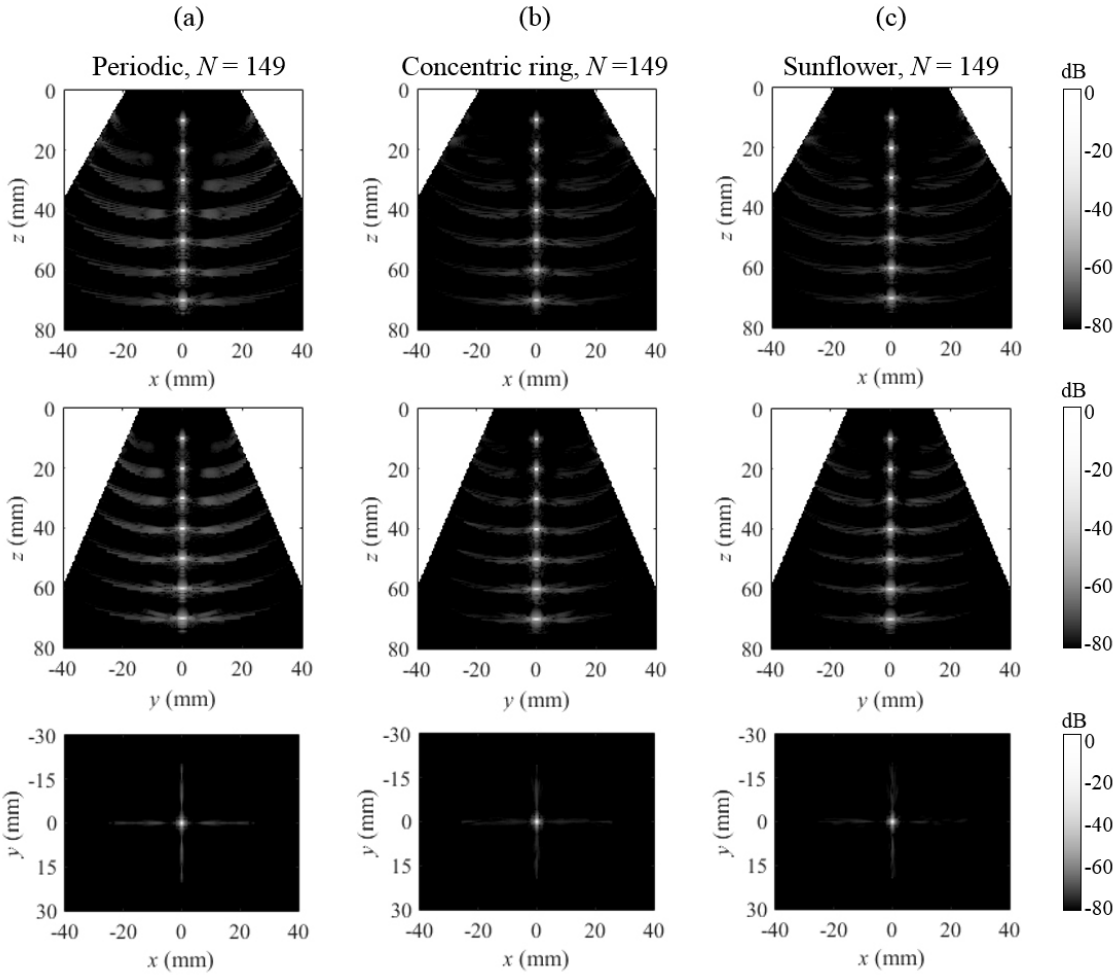

Fig. 12. The xz plane ($y = 0$), yz plane ($x = 0$), and xy plane ($z = 40$ mm) images (top to bottom) of seven-point targets at the center scanline reconstructed by using the (a) periodic, (b) concentric ring, and (c) sunflower PW patterns. The point targets are located at depths of 10, 20, 30, 40, 50, 60, and 70 mm.

to 80 dB to observe the grating lobe artifacts of the sunflower and concentric ring patterns. The artifacts of the two aperiodic PW sets [Fig. 12(b) and (c)] were approximately 10 dB lower than those of the periodic set [Fig. 12(a)].

Note that the RDF is employed with a rectangular 2-D array, as shown in Fig. 1. Then, the receive beam pattern must have a higher sidelobe pattern along the x- and y-axes than along any other direction in the xy plane [17]. Therefore, the grating lobes in the TX beam patterns of the 3-D PWSF will be less suppressed along the x- and y-directions when multiplied by the receive beam pattern, which explains why grating lobe artifacts are observed only along the x- and y-axes in Figs. 11 and 12.

Fig. 13 shows 3-D images of the second phantom. The same three PW sets as used for Figs. 11 and 12 were employed, and the dynamic range was set to 60 dB. For each of these 3-D images, the three cross-sectional images are also displayed in Fig. 14: xz, yz, and xy plane images with a dynamic range of 80 dB. Figs. 13 and 14 show that the grating lobe artifacts are also reduced for the point scatterers on the steered scanlines.

2) Contrast and Spatial Resolution Versus Depth: Fig. 15(a) and (b) show the contrast curves for point targets on the center scanline ($\theta = 0°$, $\phi = 0°$) and the steered scanline ($\theta = 30°$, $\phi = 0°$), respectively, when $N = 149$ for all PW sets. Note that the aperiodic PW sets yield higher contrasts than the periodic PW set at almost all depths on both the center and steered scanlines, and the greatest contrast improvement is 6.0 dB for the center scanline and 6.1 dB for the steered scanline. In the case of the steered scanline [Fig. 15(b)], the concentric ring pattern seems to be advantageous relative to the sunflower pattern for all depths.

On the other hand, the lateral and elevational resolutions for the point targets on the center scanline [Fig. 15(c)] and the steered scanline [Fig. 15(d)] do not exhibit noticeable differences between the PW patterns. This observation is particularly true for the elevational resolution (dotted lines). In the case of the lateral resolution (solid lines), the concentric ring pattern provides slightly improved results at near depths in Fig. 15(c) because the concentric ring pattern has a slightly narrower beamwidth due to the larger effective range of PW directions in the $\alpha\beta$-domain, as described in Section IV-A2. Obviously, such an improvement would also be obtained in the elevational direction if we used a 2-D array with a larger elevational width.

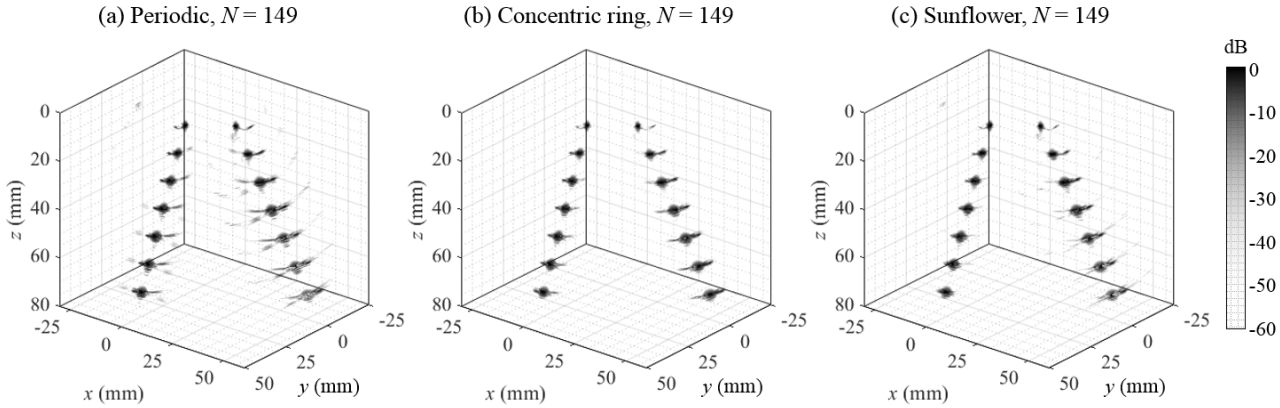

Fig. 13. 3-D images of two columns of point targets reconstructed using the (a) periodic, (b) concentric ring, and (c) sunflower PW patterns. The point targets are located at depths of 10, 20, 30, 40, 50, 60, and 70 mm.

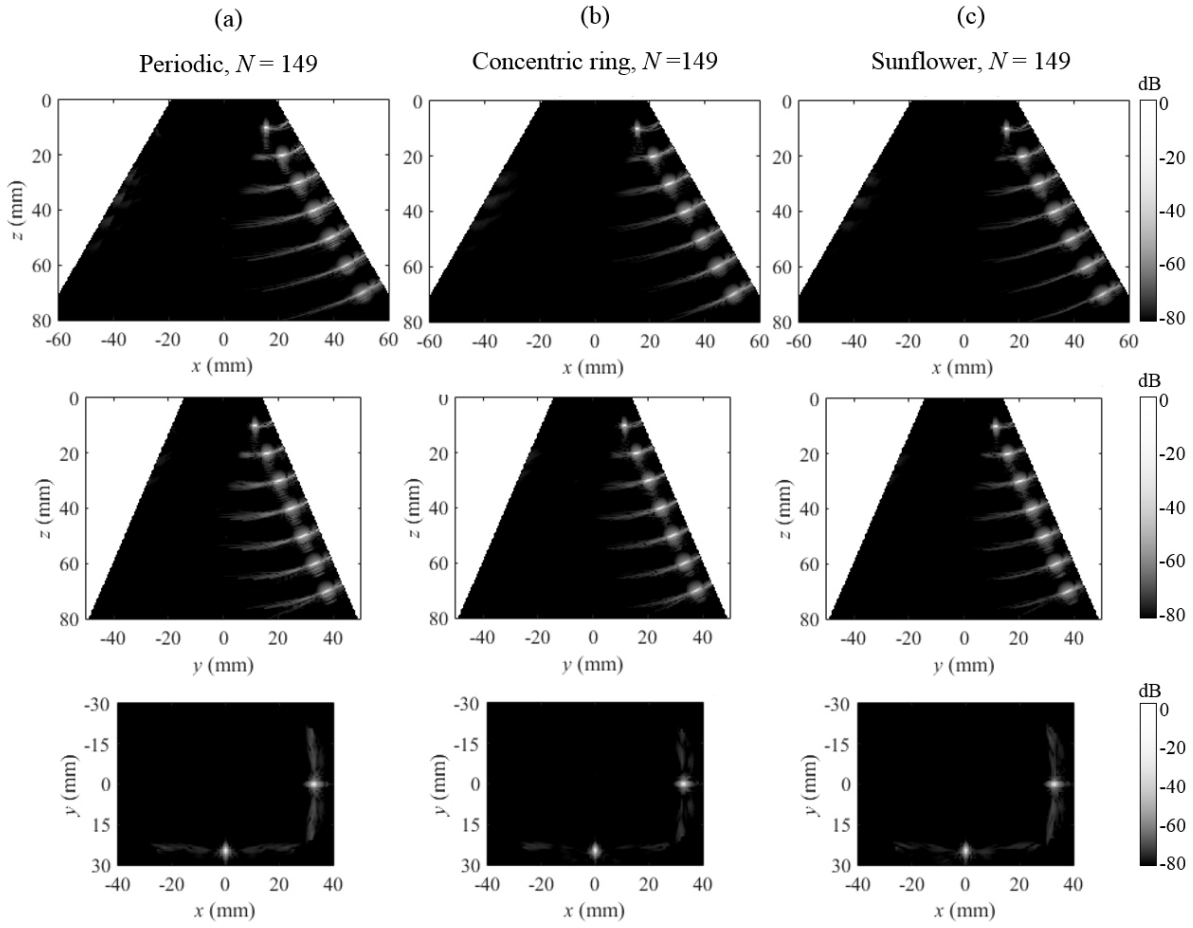

Fig. 14. The xz plane ($y = 0$), yz plane ($x = 0$), and xy plane ($z = 40$ mm) images (top to bottom) of two columns of point targets reconstructed by using the (a) periodic, (b) concentric ring, and (c) sunflower PW patterns. The point targets are located at depths of 10, 20, 30, 40, 50, 60, and 70 mm.

In Fig. 15, the spatial resolution and contrast for all PW sets deteriorated with the depth along both scanlines. This result is caused by the phenomenon in which the number of available PWs (or, equivalently, PW angles) decreases with depth, as observed in Fig. 8. Fig. 8(g)–(i) shows the case of a focal point on a side scanline, where the active seeds not only decreased in number but also lost the unique pattern of each PW set. Similarly, the contrast differences between the aperiodic PW sets and the periodic PW set decreased after 40 mm in Fig. 15(b).

In Fig. 15(c), the lateral resolution is better than the elevational resolution at depths greater than 20 mm because the lateral width of the 2-D array is greater than the elevational width. However, in Fig. 15(d), better resolution is obtained in

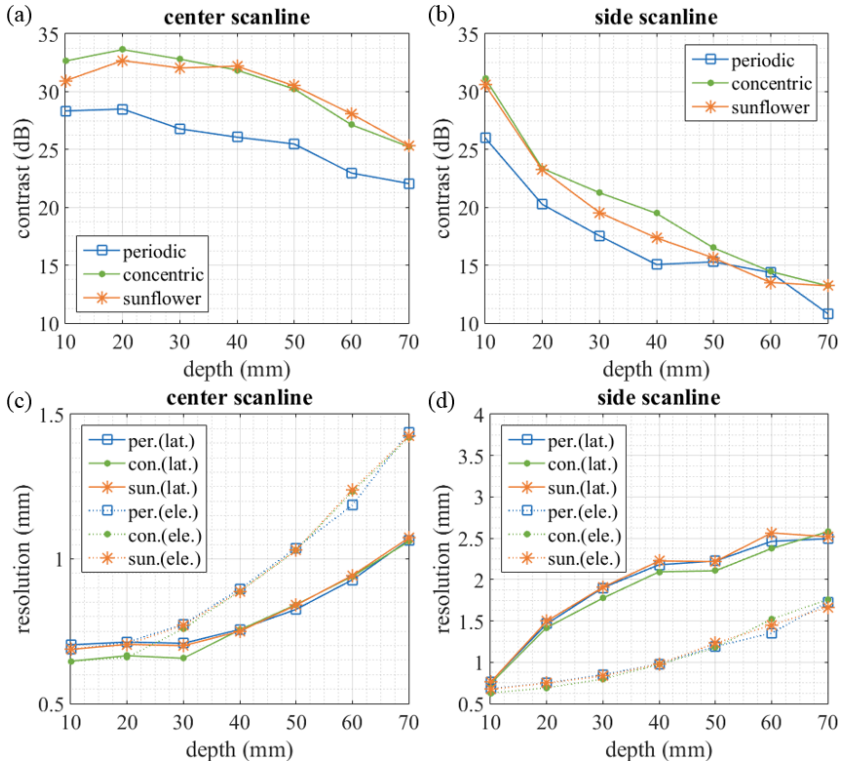

Fig. 15. (a) and (b) Contrast and (c) and (d) lateral (lat.) and elevational (ele.) resolutions measured at the (a) and (c) center scanline and the (b) and (d) laterally steered side scanline as a function of depth when using the periodic (per.), concentric ring (con.), and sunflower (sun.) sets.

the elevational direction at all depths because the range of α becomes smaller than the range of β for imaging points on the scanline that is tilted toward only the positive x-axis ($\theta = 30°$, $\phi = 0°$).

3) Contrast and Spatial Resolution Versus the Number of PWs: In Fig. 16, the contrast and spatial resolution obtained with the three PW sets measured for point targets on the center scanline are plotted as a function of the number of PWs: $N = 13$, 29, 49, 81, 113, 197, 253, 313, 377, 441, 529, 613, and 705. In Fig. 16(a)–(c), the contrast increases for all PW sets as N increases. This finding can be explained by the beam patterns in Figs. 8 and 9, which show the increasing distance between the main lobe and the grating lobe with increasing N. Fig. 16(a)–(c) demonstrates that aperiodic PW sets provide better contrast at all depths ($z = 20$, 40, and 60 mm) than the periodic PW set for all $N > 13$. They also show that the aperiodic angle sets require approximately 2–6 times fewer PWs than the periodic angle set for the same contrast. As an example, to obtain a contrast of 30 dB at $z = 40$ mm, the periodic PW set requires more than 377 PWs, whereas 81 PWs are enough when using the concentric or sunflower sets.

In contrast, Fig. 16(d)–(f) shows that the spatial resolution tends not to change with N when $N > 100$, except when the concentric ring pattern is used at a shallow depth [Fig. 16(d)]. This result indicates again that the resolution depends on the range of PWs in $\alpha\beta$-space and not on the number of PWs or the type of PW pattern. The reason for the fluctuation in Fig. 16(d)–(f) when $N < 100$ is that the effective angular range slightly changes with N due to the low density of seeds.

Only in Fig. 16(d) does the concentric ring pattern exhibit a better resolution than the other patterns. At 20 mm, Figs. 8 and 9 show that all the transmitted PWs are compounded [i.e., $\mathbb{S}(\mathbf{x}_f) = \mathbb{T}$] for all direction sets. As discussed earlier, the concentric ring has more seeds at the boundary ($r = r_0$) than the periodic or sunflower pattern, which gives it a slightly larger effective range of PW directions compared with the other patterns. Obviously, the difference in the effective range between the concentric ring and other patterns decreases as N increases because the interseed interval decreases with increasing N. Consequently, the resolution of the concentric ring becomes closer to that of other patterns with increasing N, as shown in Fig. 16(d).

V. Discussion

In this article, we proposed the aperiodic patterns of PW angles to enhance the contrast and the volume rate of 3-D PWI. Both the theoretical analysis and simulation results showed that the grating lobe levels in the synthetic TX beam patterns by the two aperiodic angle sets (concentric ring and sunflower patterns) were smaller than those by the conventional periodic angle set when the same number of PWs was used. Simulation studies also demonstrated that the aperiodic patterns enhance the contrast of 3-D PWI by approximately 3–6 dB over all depths. This result implies that the aperiodic angle sets can increase the volume rate by approximately 2–6 times

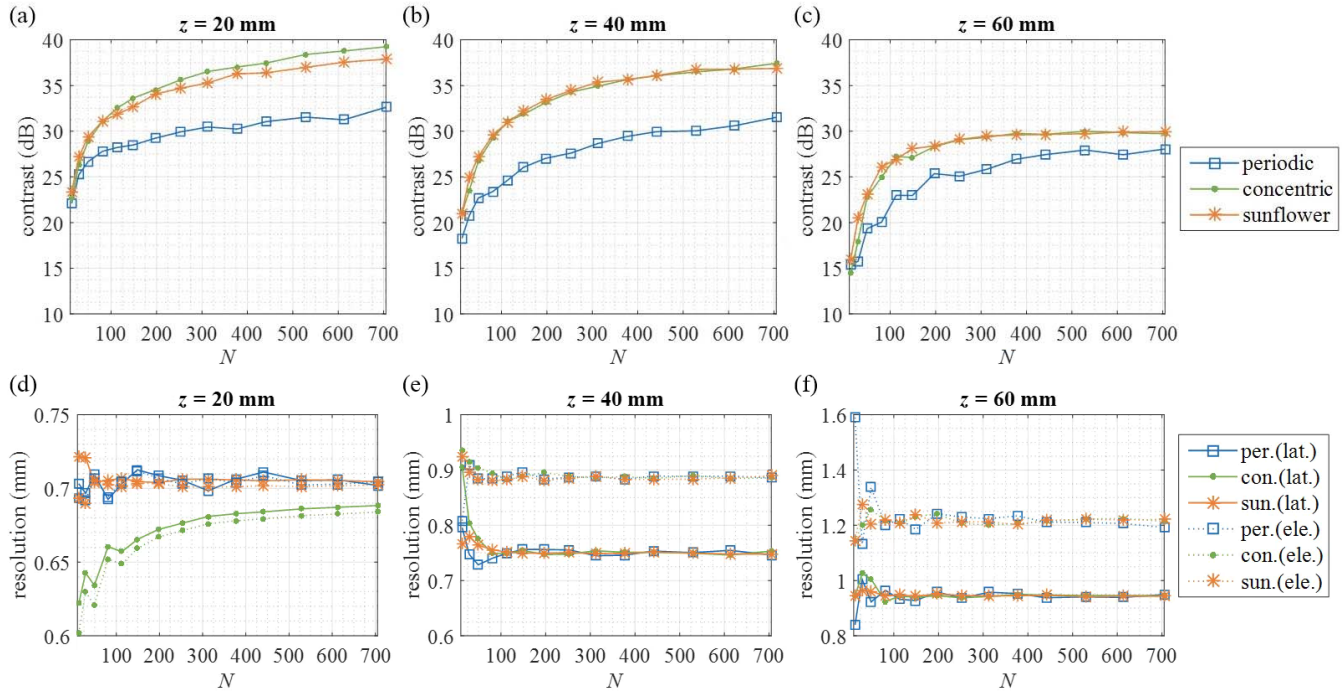

Fig. 16. (a)–(c) Contrast and (d)–(f) lateral (lat.) and elevational (ele.) resolutions measured at (a) and (d) $z = 20$ mm, (b) and (e) $z = 40$ mm, and (c) and (f) $z = 60$ mm on the center scanline as a function of the number of transmitted PWs (N) when using the periodic, concentric ring, and sunflower sets. Note that the scales of the resolution axes of (d)–(f) are different.

compared to the periodic angle set at the same contrast and spatial resolution.

A. Effect of Broadband and Array Sampling on TX Beam Pattern

In Sections III-C and IV-A, the TX beam patterns were investigated only for the cases where monochromatic (continuous) waves are transmitted. To see the effect of broadband excitation in the proposed method, the broadband TX beam patterns for the same matrix array transducer that was used in Section III-D were obtained. Specifically, PSF images of a point target at (0, 0, 20 mm) were obtained by using all the array elements for PW transmission and a single (center) element for the reception. A one-cycle pulse with a center frequency of 3 MHz was used for the PW transmission.

Fig. 17(a) shows the xy plane of broadband (pulsed-wave) beam patterns of the periodic, concentric, and sunflower angle sets when the number of PWs (N) is 81, 149, and 253. Compared to the corresponding CW beam patterns [Figs. 8(a)–(c) and 9], the grating lobes in the broadband beam patterns [Fig. 17(a)] are smudged, and the peak amplitudes of the grating lobes are decreased by 13–28 dB. Nevertheless, the broadband beam patterns were influenced by the number and distribution of the PW angles in a similar manner as in the CW beam patterns: 1) the distance between the grating lobe and the main lobe increases with the number of PWs (N) and 2) the periodic angle sets generated more isolated and stronger grating lobes than those of the concentric and sunflower sets. In Fig. 17(a), the peak magnitudes of the grating lobes of the periodic sets were approximately 4, 7, and 9 dB higher than those of the aperiodic sets (concentric and sunflower) for $N = 81$, 149, and 253, respectively. When the broadband beam patterns were observed in the xz plane [Fig. 17(b)], the peak grating lobe magnitudes of the periodic sets were approximately 7, 11, and 9 dB higher than those of the aperiodic sets for $N = 81$, 149, and 253, respectively.

Finally, it is also worth noting that edge waves radiated from the edges of a finite 2-D aperture could cause artifacts such as contrast degradation and axial grating lobes. Such artifacts can be reduced by employing tapered TX apertures, as suggested in [30]. Throughout this article, however, the amplitude apodization was not applied on the transmission to investigate the beam patterns and point target images, as well as such artifacts, for the periodic and two aperiodic PW angular patterns.

B. Varieties of PW Direction Sets

Among the aperiodic sets, the concentric ring pattern exhibited a slightly better image quality in the side region than in the sunflower pattern. Because the performance in terms of resolution and contrast differs between the aperiodic PW sets, further studies should be performed to identify better or optimal patterns for the 3-D PWSF. Furthermore, the pattern could be optimized for the receive beam pattern.

In the process of synthetic focusing, we employed as many PWs as possible for the best resolution and contrast at each imaging point. Therefore, the range of active seeds in the $\alpha\beta$ plane was much larger for the imaging points in the center region than for those in the side region as in Fig. 8, which resulted in better resolution in the central region. If a uniform

resolution over the scan volume is required, the same N_s could be used for all imaging points. In addition, the image quality of the side regions can be improved by concentrating seeds near the boundary of r_0 in the $\alpha\beta$ plane, although this approach may compromise the image quality in the center region.

We employed PW patterns with a circular boundary in this article for the convenience of analysis of the synthetic TX beam pattern. If a square boundary is employed, the image quality in the corners will be improved, although it happens at the expense of the volume rate and computational complexity.

C. Comparison With Scanline-Based Imaging Methods

As PWSF enables synthetic and dynamic focusing in transmission, it is advantageous relative to other scanline-based imaging methods in terms of the volume rate and spatial resolution. Conventional focusing (CF) transmits a focused beam for every scanline in a volume. Whereas 2-D US imaging has a few hundred scanlines, 3-D US imaging demands thousands of scanlines. When an imaging volume consists of 128×96 scanlines, the CF requires 1.1 s to scan the volume with a depth of 70 mm.

To reduce the scanning time, many research groups have researched MLT in which 2 or 4 simultaneous focused beams are transmitted along M different scanlines. Although MLT was proven to be feasible for 3-D echocardiography [18], [19], a twofold or fourfold enhancement in the volume rate is not enough for high-quality 3-D imaging that requires tens of thousands of scanlines.

In addition, CF and MLT employ a focused TX beam with a fixed focal depth. When using a fixed focused beam in transmission, a large F-number is generally chosen to maintain a constant resolution with depth, resulting in a loss in the overall resolution.

To qualitatively compare the 3-D PWSF with the scanline-based imaging methods (CF and MLT), volume images of 45 point targets were acquired by using 3-D PWSF schemes with three PW angle sets, CF, 4-MLT, and 16-MLT, as shown in Fig. 18. In M-MLT, M scanlines are obtained at the same time by transmitting M focused beams. The transverse diagonal scheme proposed to reduce the crosstalk between TX beams in [17] was applied to obtain the 4-MLT image. The scheme was not able to be employed for 16-MLT because of the large number of TX beams; thus, the normal MLT scheme was used for 16-MLT. For CF and MLT, the F-number was 3 and the focal depth was 40 mm in transmission. For all the methods, the same dynamic receive focusing was applied.

On the top of each subfigure of Fig. 18, the number of transmissions for each method is presented. The PWSF images exhibit high-resolution point targets because of the dynamic focusing in transmission, whereas CF and MLT provide low-resolution images due to the fixed focusing. Compared to the 16-MLT image [Fig. 18(c)], the concentric and sunflower PWSF images [Fig. 18(e) and (f)] have a better overall resolution, fewer artifacts, and a more than twofold higher volume rate.

D. Computational Complexity and Implementation

By using the proposed aperiodic PW sets, the computational expense for beamforming as well as the required number of PWs can be reduced. However, the 3-D PWSF scheme still requires much more computation than CF and MLT for the reconstruction of a given volume. Whereas CF requires one beamforming process per imaging point, PWSF needs dozens or hundreds of beamformations for each imaging point to synthesize multiple PWs. As the number of beamformations in PWSF varies with the imaging point, we calculated the average number of beamformations per point, $\bar{N}_s$; $1 < \bar{N}_s < N$. The total number of beamforming processes for reconstructing a volume in PWSF, $N_{\mathrm{s,tot}}$, can be expressed as follows:

$$N_{\mathrm{s,tot}} = \sum_{j=1}^{N_{\mathrm{img}}} N_s(j) \tag{19}$$

where N_{img} is the total number of imaging points within the volume and $N_{\mathrm{s}}(j)$ is the number of synthesized PWs (i.e., the number of beamformations) for the jth imaging point. The average number of beamforming processes per point is obtained by $\bar{N}_s = N_{\mathrm{s,tot}}/N_{\mathrm{img}}$. Whereas CF requires one beamformation per point, PWSF demands $\bar{N}_s$ beamformations per point. That is, PWSF requires an $\bar{N}_s$ times higher computational cost than CF for the reconstruction of the same volume. $\bar{N}_s$ is obviously proportional to the number of transmitted PWs (N). For the experimental setup used in Fig. 18, $\bar{N}_s$ was approximately $0.34N$, which means that when $N = 313$, PWSF demands 107 times more computation than CF. In addition, it requires a much higher computation rate than CF considering its higher volume rate for real-time implementation.

Reducing the computational complexity for real-time 3-D PWSF is of crucial importance. The proposed aperiodic sets are also attractive in terms of the computational cost because they provide similar resolution and contrast using a smaller number of PWs compared to the periodic PW set. Moreover, $\bar{N}_s$ can be further lowered by reducing $N_{\mathrm{s}}(j)$ in (19) for imaging points in the center image area to achieve a uniform resolution. In addition, the base-band beamformer with phase rotation can be employed for computational complexity reduction because it utilizes a lower sampling rate than the RF beamformer [40], [41]. The Fourier-domain beamformer can also be used to reduce the complexity of PWSF [42], [43]. Nevertheless, 3-D PWSF would still demand large amounts of computational power. The most practical approach for meeting this requirement is to utilize parallel processors, such as multicore DSPs [44] or GPUs [45].

In this article, we used a base-band beamformer and utilized GPUs via the CUDA platform. Approximately 8.6 min were required to reconstruct a volume with a depth of 70 mm on a personal computer equipped with a GeForce 1080 GTX (NVIDIA Corporation, Santa Clara, CA, USA), Intel Core i7-4790 (Intel Corporation, Santa Clara, CA, USA), and 32-GB RAM. Three-dimensional PWSF at this processing speed can only be used in offline reconstruction environments, such as CT or MR imaging. Hence, the fast implementation of 3-D PWSF represents an important research topic, and

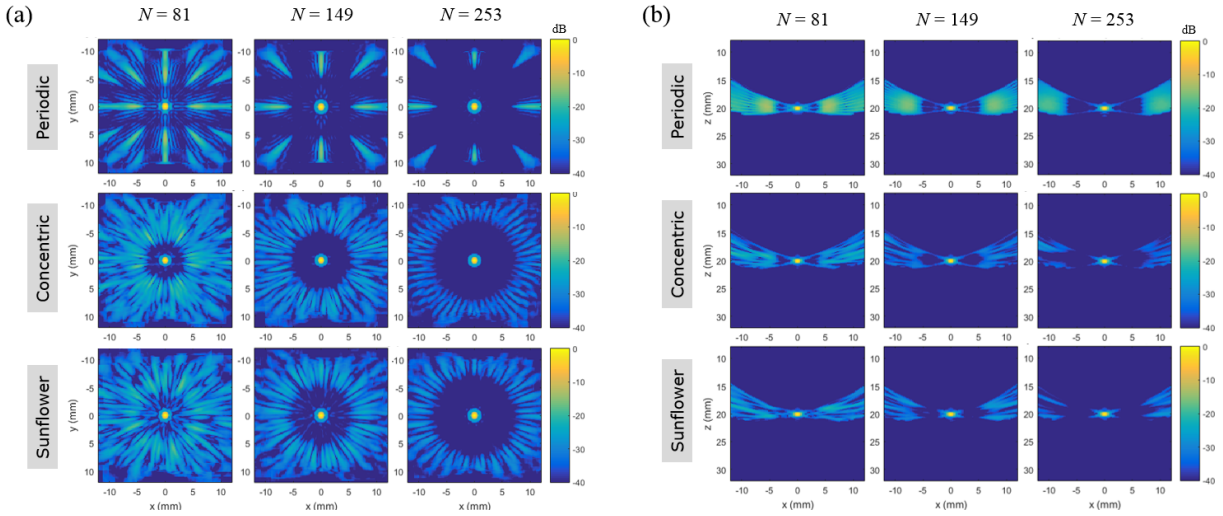

Fig. 17. (a) The *xy* planes and (b) *xz* planes of 3-D broadband TX beam patterns when using PW angles of periodic, concentric ring, and sunflower patterns (from top to bottom rows). On the top of each column, the number of PWs used is presented.

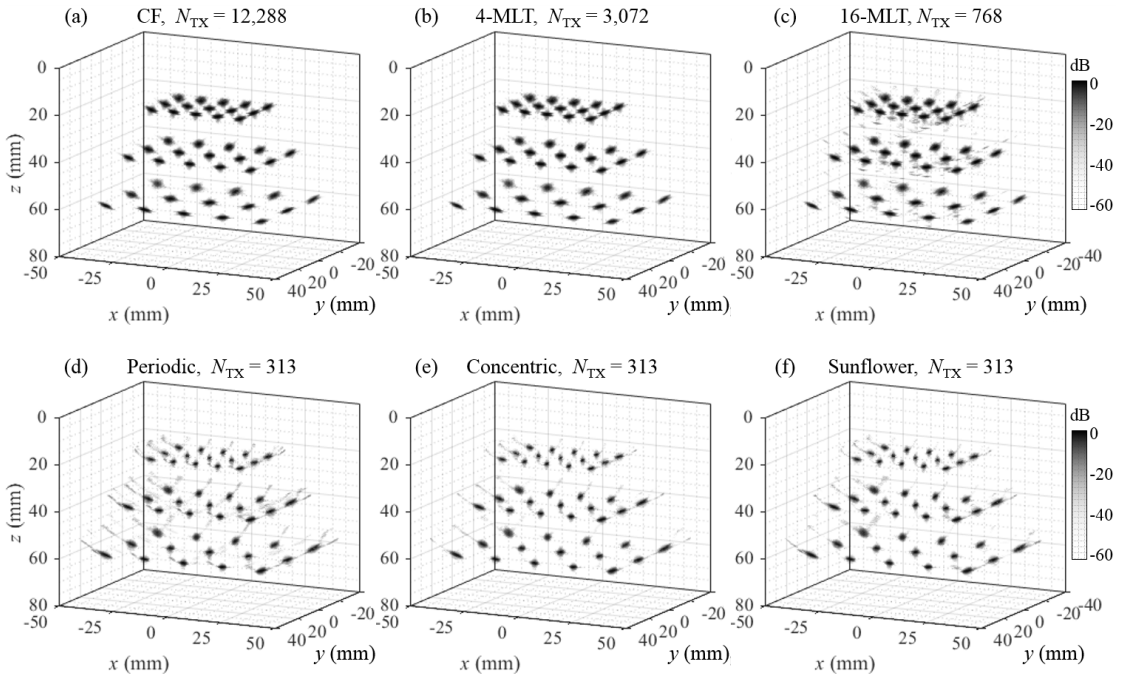

Fig. 18. 3-D PSF images of 45-point targets reconstructed using (a) CF, (b) 4-MLT, (c) 16-MLT and 3-D PWSF with the (d) periodic, (e) concentric ring, and (f) sunflower PW direction sets. N_{TX} is the number of transmissions. On top of each subfigure, the number of transmissions for each method is presented.

real-time reconstruction may be possible in the near future as the performance of parallel processing devices continues to increase at a high growth rate.

E. Effect of Motion

The motion artifact problem must be considered in 3-D PWSF because dozens or sometimes even hundreds of PWs must be coherently compounded. Therefore, we need to assess the effect of motion and reduce the motion artifacts in 3-D PWSF. A decrease in the required number of PWs using the proposed method will be helpful for reducing the motion artifacts in 3-D PWI since the incoherence caused by the motion would decrease as the number of synthetic PWs decreases. In addition, some motion compensation techniques that have been proposed for 2-D synthetic focusing can be applied to 3-D PWSF. For instance, B. Denarie *et al.* [27] suggested a polarity-alternating TX sequence to mitigate the lateral shift effect due to the radial motion in 2-D PWI. Further investigation into the optimization of the TX sequence (the order of transmission of PWs) for 3-D PWI will enable the reduction of motion artifacts. Similarly, other motion correction algorithms developed for diverging wave or synthetic aperture imaging can also be applied to 3-D PWSF [46]–[49].

F. Signal-to-Noise Ratio

Although the proposed aperiodic PW sets enhance the volume rate compared with the periodic PW set without sacrificing resolution and contrast, this method cannot prevent a decrease in the signal-to-noise ratio (SNR) when using a small number of PWs. However, various SNR enhancement techniques can be utilized along with the proposed method. For example, we can employ the coded excitation techniques to transmit PWs encoded by the chirp or Barker code [50], [51]. Multiplane-wave imaging based on the Hadamard matrix [52]–[54] can also be utilized to improve the SNR of 3-D PWSF imaging with an aperiodic PW set. Such multiplane imaging methods will also be helpful to reduce the large number of transmissions in the proposed 3-D PWSF method.

VI. Conclusion

A 3-D PWSF method has been suggested to achieve a high contrast and a high volume rate. In this method, an aperiodic PW angle set is employed instead of a periodic angle set to reduce the grating lobe level in 3-D PWI. We proposed two patterns as the aperiodic PW angle set: concentric ring and sunflower patterns. In the TX beam patterns, the grating lobe levels are reduced by 11.4 dB at a depth of 20 mm and by at least 7.2 dB at a depth of 50 mm when using the proposed pattern. Simulation studies show that the use of aperiodic patterns enhances the contrast of 3-D PWI by approximately 3–6 dB over all depths. In addition, for the same contrast and spatial resolution, the aperiodic sets require approximately 2–6 times fewer PWs than the periodic set.

Appendix A

The ultrasonic 2-D beam pattern on the xy plane is expressed by the 2-D Fourier transform of $p_s(\alpha, \beta)$, which is the distribution of compounded PW angles, as presented in (6). Applying the polar coordinate transformations (see Fig. 2) to the Fourier transform in (6), the beam pattern can be rewritten as follows:

$$\Psi(\rho, \theta_\rho) = \int_0^\infty \int_0^{2\pi} p_s(r, \theta_r) e^{-jk\rho r \cos(\theta_r - \theta_\rho)} r\, dr\, d\theta_r \quad \text{(A1)}$$

because $\alpha x + \beta y = \rho r \cos(\theta_r - \theta_\rho)$. The Fourier transform of a circularly symmetric function is itself circularly symmetric and becomes a particular form that is referred to as a Fourier–Bessel transform [55]. Since p_s in (7) is circularly symmetric, (A1) can be expressed by

$$\Psi(\rho) = 2\pi \int_0^\infty r p_s(r) J_0(k\rho r) dr \quad \text{(A2)}$$

where J_0 is a Bessel function of the first kind, of zero order, which is

$$J_0(k\rho r) = \frac{1}{2\pi} \int_0^{2\pi} e^{-jk\rho r \cos(\theta_r - \theta_\rho)} d\theta_r. \quad \text{(A3)}$$

Substituting (7) into (A2) and replacing $k\rho r$ with r', the beam pattern can be written as follows:

$$\begin{aligned} \Psi(\rho) &= 2\pi \int_0^{r_0} r J_0(k\rho r) dr \\ &= \frac{2\pi}{k^2\rho^2} \int_0^{k\rho r_0} r' J_0(r') dr' \\ &= \frac{2\pi r_0}{k\rho} J_1(k\rho r_0) \end{aligned} \quad \text{(A4)}$$

where J_1 is a Bessel function of the first kind, of order 1. Since the jinc function is defined as

$$\text{jinc}(a) = \frac{2J_1(\pi a)}{\pi a} \quad \text{(A5)}$$

the beam pattern synthesized by using PWs with a range of $r < r_0$ is

$$\Psi(\rho) = \pi r_0^2 \text{jinc}(2r_0\rho/\lambda). \quad \text{(A6)}$$

Appendix B

Assume that there are $P-1$ concentric rings with a constant radial increment of d_r and seeds are distributed on each pth ring ($p = 1, 2, \ldots, P-1$) with a constant arc length interval of $d_c[p]$, as in Fig. 5(a). Note that $d_c[p] = d_\theta[p] d_r p$, where $d_\theta[p]$ and $d_r p$ are the angle intervals between two adjacent seeds and the radius of the pth concentric ring, respectively. The total number of seeds including a seed at the origin is then

$$N = \sum_{p=0}^{P-1} Q[p] = 1 + \sum_{p=1}^{P-1} \frac{2\pi d_r p}{d_c[p]} \quad \text{(B1)}$$

where $Q[p]$ is the number of seeds in the pth ring and $Q[0]$ represents the seed at the origin ($Q[0] = 1$). To achieve the highest uniformity of the seed distribution, the arc length interval $d_c[p]$ for all p should be close to the radial interval d_r. Assuming that $d_c[p] = d_r$, the total number of seeds in (B1) can then be expressed as follows:

$$N \approx 1 + \sum_{p=1}^{P-1} 2\pi p = \pi P^2 - \pi P + 1. \quad \text{(B2)}$$

Using the quadratic formula, the number of concentric rings for the uniform distribution of seeds is obtained as follows:

$$P = \text{round}\left(\frac{1 + \sqrt{1 + 4(N-1)/\pi}}{2} \right). \quad \text{(B3)}$$

Once P is determined, d_r is given by

$$d_r = r_0/(P-1) \quad \text{(B4)}$$

where r_0 is the range of PW angles and the radius of the largest ring.

Now, let us consider a more realistic case in which $d_c[p] = d_c' \neq d_r$. Then, (B1) becomes

$$N \approx 1 + \sum_{p=1}^{P-1} \frac{2\pi d_r p}{d_c'} = \frac{2\pi d_r}{d_c'} \frac{P(P-1)}{2} + 1. \quad \text{(B5)}$$

From (B5), $d'_{\mathrm{c}} = \pi d_{\mathrm{r}} P(P-1)/(N-1)$, and the number of seeds on the pth ring is expressed as follows:

$$Q[p] = \mathrm{round}\left(2\pi d_r\, p/d'_{\mathrm{c}}\right). \tag{B6}$$

Finally, the angular interval $d_\theta[p]$ and the arc length interval $d_{\mathrm{c}}[p]$ between two adjacent seeds on the pth ring are

$$d_\theta[p] = 2\pi / Q[p] \tag{B7}$$

and

$$d_{\mathrm{c}}[p] = 2\pi d_r\, p/Q[p]. \tag{B8}$$

REFERENCES

[1] A. Fenster, G. Parraga, and J. Bax, "Three-dimensional ultrasound scanning," *Interface Focus*, vol. 1, no. 4, pp. 503–519, 2011.

[2] J. Provost *et al.*, "3D ultrafast ultrasound imaging *in vivo*," *Phys. Med. Biol.*, vol. 59, no. 19, pp. L1–L13, 2014.

[3] A. Kyei-Mensah, J. Zaidi, R. Pittrof, A. Shaker, S. Campbell, and S.-L. Tan, "Transvaginal three-dimensional ultrasound: Accuracy of follicular volume measurements," *Fertility Sterility*, vol. 65, no. 2, pp. 371–376, 1996.

[4] F.-M. Chang *et al.*, "Three-dimensional ultrasound assessment of fetal liver volume in normal pregnancy: A comparison of reproducibility with two-dimensional ultrasound and a search for a volume constant," *Ultrasound Med. Biol.*, vol. 23, no. 3, pp. 381–389, 1997.

[5] M. Bossard *et al.*, "Conventional versus 3-D echocardiography to predict arrhythmia recurrence after atrial fibrillation ablation," *J. Cardiovascular Electrophysiol.*, vol. 28, no. 6, pp. 651–658, 2017.

[6] M. Biswas *et al.*, "Two- and three-dimensional speckle tracking echocardiography: Clinical applications and future directions," *Echocardiography*, vol. 30, no. 1, pp. 88–105, 2013.

[7] J. Crosby, B. H. Amundsen, T. Hergum, E. W. Remme, S. Langeland, and H. Torp, "3-D speckle tracking for assessment of regional left ventricular function," *Ultrasound Med. Biol.*, vol. 35, no. 3, pp. 458–471, Mar. 2009.

[8] J.-L. Gennisson *et al.*, "4-D ultrafast shear-wave imaging," *IEEE Trans. Ultrason., Ferroelectr., Freq. Control*, vol. 62, no. 6, pp. 1059–1065, Jun. 2015.

[9] C. Rabut, V. Finel, M. Correia, M. Pernot, T. Deffieux, and M. Tanter, "Full 4D functional ultrasound imaging in rodents using a matrix array," in *Proc. IEEE Int. Ultrason. Symp.*, Sep. 2017, p. 1.

[10] L. Song, C. Kim, K. Maslov, K. K. Shung, and L. V. Wang, "High-speed dynamic 3D photoacoustic imaging of sentinel lymph node in a murine model using an ultrasound array," *Med. Phys.*, vol. 36, no. 8, pp. 3724–3729, 2009.

[11] D. P. Shattuck, M. D. Weinshenker, S. W. Smith, and O. T. von Ramm, "Explososcan: A parallel processing technique for high speed ultrasound imaging with linear phased arrays," *J. Acoust. Soc. Amer.*, vol. 75, no. 4, pp. 1273–1282, 1984.

[12] O. T. von Ramm, S. W. Smith, and H. G. Pavy, "High-speed ultrasound volumetric imaging system—Part II: Parallel processing and image display," *IEEE Trans. Ultrason., Ferroelectr., Freq. Control*, vol. 38, no. 2, pp. 109–115, Mar. 1991.

[13] T. Hergum, T. Bjastad, K. Kristoffersen, and H. Torp, "Parallel beamforming using synthetic transmit beams," *IEEE Trans. Ultrason., Ferroelectr., Freq. Control*, vol. 54, no. 2, pp. 271–280, Feb. 2007.

[14] A. Rabinovich, Z. Friedman, and A. Feuer, "Multi-line acquisition with minimum variance beamforming in medical ultrasound imaging," *IEEE Trans. Ultrason., Ferroelectr., Freq. Control*, vol. 60, no. 12, pp. 2521–2530, Dec. 2013.

[15] L. Tong, H. Gao, H. F. Choi, and J. D'hooge, "Comparison of conventional parallel beamforming with plane wave and diverging wave imaging for cardiac applications: A simulation study," *IEEE Trans. Ultrason., Ferroelectr., Freq. Control*, vol. 59, no. 8, pp. 1654–1663, Aug. 2012.

[16] B. Madore, P. J. White, K. Thomenius, and G. T. Clement, "Accelerated focused ultrasound imaging," *IEEE Trans. Ultrason., Ferroelectr., Freq. Control*, vol. 56, no. 12, pp. 2612–2623, Dec. 2009.

[17] B. Denarie, T. Bjastad, and H. Torp, "Multi-line transmission in 3-D with reduced crosstalk artifacts: A proof of concept study," *IEEE Trans. Ultrason., Ferroelectr., Freq. Control*, vol. 60, no. 8, pp. 1708–1718, Aug. 2013.

[18] L. Tong, A. Ramalli, R. Jasaityte, P. Tortoli, and J. D'Hooge, "Multi-transmit beam forming for fast cardiac imaging—Experimental validation and *in vivo* application," *IEEE Trans. Med. Imag.*, vol. 33, no. 6, pp. 1205–1219, Jun. 2014.

[19] A. Ortega *et al.*, "A comparison of the performance of different multiline transmit setups for fast volumetric cardiac ultrasound," *IEEE Trans. Ultrason., Ferroelectr., Freq. Control*, vol. 63, no. 12, pp. 2082–2091, Dec. 2016.

[20] G. R. Lockwood, J. R. Talman, and S. S. Brunke, "Real-time 3-D ultrasound imaging using sparse synthetic aperture beamforming," *IEEE Trans. Ultrason., Ferroelectr., Freq. Control*, vol. 45, no. 4, pp. 980–988, Jul. 1998.

[21] M. F. Rasmussen and J. A. Jensen, "Comparison of 3-D synthetic aperture phased-array ultrasound imaging and parallel beamforming," *IEEE Trans. Ultrason., Ferroelectr., Freq. Control*, vol. 61, no. 10, pp. 1638–1650, Oct. 2014.

[22] M. Yang, R. Sampson, S. Wei, T. F. Wenisch, and C. Chakrabarti, "High frame rate 3-D ultrasound imaging using separable beamforming," *J. Signal Process. Syst.*, vol. 78, no. 1, pp. 73–84, Aug. 2014.

[23] P. Santos, G. U. Haugen, L. Løvstakken, E. Samset, and J. D'hooge, "Diverging wave volumetric imaging using subaperture beamforming," *IEEE Trans. Ultrason., Ferroelectr., Freq. Control*, vol. 63, no. 12, pp. 2114–2124, Dec. 2016.

[24] J.-J. Kim and T.-K. Song, "Real-time 3D imaging methods using 2D phased arrays based on synthetic focusing techniques," *Ultrason. Imag.*, vol. 30, no. 3, pp. 169–188, 2008.

[25] M. Flesch *et al.*, "4D *in vivo* ultrafast ultrasound imaging using a row-column addressed matrix and coherently-compounded orthogonal plane waves," *Phys. Med. Biol.*, vol. 62, no. 11, p. 4571, 2017.

[26] G. Montaldo, M. Tanter, J. Bercoff, N. Benech, and M. Fink, "Coherent plane-wave compounding for very high frame rate ultrasonography and transient elastography," *IEEE Trans. Ultrason., Ferroelectr., Freq. Control*, vol. 56, no. 3, pp. 489–506, Mar. 2009.

[27] B. Denarie *et al.*, "Coherent plane wave compounding for very high frame rate ultrasonography of rapidly moving targets," *IEEE Trans. Med. Imag.*, vol. 32, no. 7, pp. 1265–1276, Jul. 2013.

[28] J.-H. Chang and T.-K. Song, "A new synthetic aperture focusing method to suppress the diffraction of ultrasound," *IEEE Trans. Ultrason., Ferroelectr., Freq. Control*, vol. 58, no. 2, pp. 327–337, Feb. 2011.

[29] S. Bae and T.-K. Song, "Methods for grating lobe suppression in ultrasound plane wave imaging," *Appl. Sci.*, vol. 8, no. 10, p. 1881, Oct. 2018.

[30] J. Jensen, M. Stuart, and J. Jensen, "Optimized plane wave imaging for fast and high quality ultrasound imaging," *IEEE Trans. Ultrason., Ferroelectr., Freq. Control*, vol. 63, no. 11, pp. 1922–1934, Nov. 2016.

[31] C. Tekes, M. Karaman, and F. L. Degertekin, "Optimizing circular ring arrays for forward- looking IVUS imaging," *IEEE Trans. Ultrason., Ferroelectr., Freq. Control*, vol. 58, no. 12, pp. 2596–2607, Dec. 2011.

[32] J. N. Ridley, "Packing efficiency in sunflower heads," *Math. Biosci.*, vol. 58, no. 1, pp. 129–139, Feb. 1982.

[33] M. C. Viganó, G. Toso, G. Caille, C. Mangenot, and I. E. Lager, "Sunflower array antenna with adjustable density taper," *Int. J. Antennas Propag.*, vol. 2009, Jan. 2009, Art. no. 624035.

[34] O. Martínez-Graullera, C. J. Martín, G. Godoy, and L. G. Ullate, "2D array design based on Fermat spiral for ultrasound imaging," *Ultrasonics*, vol. 50, no. 2, pp. 280–289, 2010.

[35] A. Ramalli, E. Boni, A. S. Savoia, and P. Tortoli, "Density-tapered spiral arrays for ultrasound 3-D imaging," *IEEE Trans. Ultrason., Ferroelectr., Freq. Control*, vol. 62, no. 8, pp. 1580–1588, Aug. 2015.

[36] S. Bae, P. Kim, and T.-K. Song, "Ultrasonic sector imaging using plane wave synthetic focusing with a convex array transducer," *J. Acoust. Soc. Amer.*, vol. 144, no. 5, pp. 2627–2644, 2018.

[37] S. F. Liew, H. Noh, J. Trevino, L. D. Negro, and H. Cao, "Localized photonic band edge modes and orbital angular momenta of light in a golden-angle spiral," *Opt. Express*, vol. 19, no. 24, pp. 23631–23642, 2011.

[38] J. A. Jensen, "Field: A program for simulating ultrasound systems," in *Proc. 10th Nordic-Baltic Conf. Biomed. Imag.*, vol. 34, 1996, pp. 351–353.

[39] K. F. Üstüner and G. L. Holley, "Ultrasound imaging system performance assessment," presented at the AAPM 45th Annu. Meeting, 2003. [Online]. Available: http://www.aapm.org/meetings/03aM/pdf/9905-9858.pdf

[40] R. G. Pridham and R. A. Mucci, "Digital interpolation beamforming for low-pass and bandpass signals," *Proc. IEEE*, vol. 67, no. 6, pp. 904–919, Jun. 1979.

[41] M. Kim, G. Lee, M. Park, and T.-K. Song, "Computationally efficient architecture for ultrasound phase rotation beamforming," *Electron. Lett.*, vol. 52, no. 1, pp. 18–19, 2016.
[42] J. Cheng and J.-Y. Lu, "Extended high-frame rate imaging method with limited-diffraction beams," *IEEE Trans. Ultrason., Ferroelectr., Freq. Control*, vol. 53, no. 5, pp. 880–899, May 2006.
[43] P. Kruizinga, F. Mastik, N. de Jong, A. F. W. van der Steen, and G. van Soest, "Plane-wave ultrasound beamforming using a nonuniform fast Fourier transform.," *IEEE Trans. Ultrason., Ferroelectr., Freq. Control*, vol. 59, no. 12, pp. 2684–2691, Dec. 2012.
[44] J. Ma, K. Karadayi, M. Ali, and Y. Kim, "Ultrasound phase rotation beamforming on multi-core DSP," *Ultrasonics*, vol. 54, no. 1, pp. 99–105, Jan. 2014.
[45] B. Y. S. Yiu, I. K. H. Tsang, and A. C. H. Yu, "GPU-based beamformer: Fast realization of plane wave compounding and synthetic aperture imaging," *IEEE Trans. Ultrason., Ferroelectr., Freq. Control*, vol. 58, no. 8, pp. 71698–1705, Aug. 2011.
[46] P. Joos *et al.*, "High-frame-rate 3-D echocardiography based on motion compensation: An *in vitro* evaluation," in *Proc. IEEE Int. Ultrason. Symp.*, Sep. 2017, pp. 1–4.
[47] Y. Chen, J. D'hooge, and J. Luo, "Doppler-based motion compensation strategies for 3-D diverging wave compounding and multiplane-transmit beamforming: A simulation study," *IEEE Trans. Ultrason., Ferroelectr., Freq. Control*, vol. 65, no. 9, pp. 1631–1642, Sep. 2018.
[48] K. L. Gammelmark and J. A. Jensen, "2-D tissue motion compensation of synthetic transmit aperture images," *IEEE Trans. Ultrason., Ferroelectr., Freq. Control*, vol. 61, no. 4, pp. 594–610, Apr. 2014.
[49] K. S. Kim, J. S. Hwang, J. S. Jeong, and T. K. Song, "An efficient motion estimation and compensation method for ultrasound synthetic aperture imaging," *Ultrason. Imag.*, vol. 24, pp. 91–99, Apr. 2002.
[50] P. Song, M. W. Urban, A. Manduca, J. F. Greenleaf, and S. Chen, "Coded excitation plane wave imaging for shear wave motion detection," *IEEE Trans. Ultrason., Ferroelectr., Freq. Control*, vol. 62, no. 7, pp. 1356–1372, Jul. 2015.
[51] F. Zhao, L. Tong, Q. He, and J. Luo, "Coded excitation for diverging wave cardiac imaging: A feasibility study," *Phys. Med. Biol.*, vol. 62, no. 4, pp. 1565–1584, 2017.
[52] E. Tiran *et al.*, "Multiplane wave imaging increases signal-to-noise ratio in ultrafast ultrasound imaging," *Phys. Med. Biol.*, vol. 60, pp. 8549–8566, Nov. 2015.
[53] P. Gong, P. Song, and S. Chen, "Ultrafast synthetic transmit aperture imaging using Hadamard-encoded virtual sources with overlapping sub-apertures," *IEEE Trans. Med. Imag.*, vol. 36, no. 6, pp. 1372–1381, Jun. 2017.
[54] P. Gong, P. Song, and S. Chen, "Delay-encoded harmonic imaging (DE-HI) in multiplane-wave compounding," *IEEE Trans. Med. Imag.*, vol. 36, no. 4, pp. 952–959, Apr. 2017.
[55] J. W. Goodman, "Analysis of two-dimensional signals and systems," in *Introduction to Fourier Optics*, 2nd ed. New York, NY, USA: McGraw Hill, 1996, pp. 4–31.

Sua Bae (M'12) received the B.S., M.S., and Ph.D. degrees in electronic engineering from Sogang University, Seoul, South Korea, in 2012, 2014, and 2019, respectively.

In 2018, she was a Research Trainee with the Department of Physiology and Biomedical Engineering, Mayo Clinic, Rochester, MN, USA, for four months. She is currently a Postdoctoral Researcher with the Department of Electronic Engineering, Sogang University. Her research interest includes medical ultrasound imaging, shear wave elastography, and therapeutic ultrasound.

Dr. Bae was a recipient of the Global Ph.D. Fellowship Program scholarship from the National Research Foundation of Korea funded by the Ministry of Education, South Korea.

Jiwon Park (M'15) received the B.S. and M.S. degrees in electronic engineering from Sogang University, Seoul, South Korea, in 2015 and 2017, respectively.

She is currently an Engineer with the Controller Development Team, Samsung Electronics Company Ltd., Suwon, South Korea. Her previous research interest includes medical ultrasound microbeamforming for matrix array transducer and 3-D plane wave imaging.

Tai-Kyong Song (M'97) received the B.S. degree in electronic engineering from Sogang University, Seoul, South Korea, in 1984, and the M.S. and Ph.D. degrees in electrical and electronic engineering from the Korea Advanced Institute of Science and Technology (KAIST), Daejeon, South Korea, in 1985 and 1990, respectively.

He was a Research Fellow with the Department of Physiology and Biophysics, Mayo Clinic, Rochester, MN, USA, for two years. He was an Adjunct Professor with the Department of Information and Communication Engineering, KAIST, from 1993 to 1995. He was a Staff Scientist with Siemens Medical System Inc., Issaquah, WA, USA, from 1995 to 1997. He joined the Department of Electronic Engineering, Sogang University, as an Assistant Professor, in 1997, and was promoted to Professor in 2006, where he is currently the Director of the Sogang Future Lab and the Director of the ICT Convergence Research Center for Disaster Safety, and has been the Director of the Medical Solution Institute since 2000. His research interests include medical ultrasound imaging and therapy, ultrafast 3-D ultrasound imaging, portable ultrasound systems, and digital signal and image processing for medical ultrasound applications.

Dr. Song is a member of the National Academy of Engineering of Korea. He was an Associate Editor of the IEEE TRANSACTIONS ON ULTRASONICS, FERROELECTRICS, AND FREQUENCY CONTROL, from 2002 to 2007. In 2017, he was nominated for the Minister Prize Award of the Ministry of Science, ICT, and Future Planning, South Korea.